sustainability

MDPI

Article

Integrating GIS, Statistical, Hydrogeochemical Modeling and Graphical Approaches for Hydrogeochemical Evaluation of Ad-Dawadmi Ground Water, Saudi Arabia: Status and Implications of Evaporation and Rock–Water Interactions

Hassan E. Gomaa [1,2,*], AbdAllah A. Alotibi [1], Mohamed Charni [3,4] and Fatma A. Gomaa [1,5,*]

[1] Department of Chemistry, College of Science and Humanities, Shaqra University, Ad-Dawadmi 11911, Saudi Arabia; aaalotaibi@su.edu.sa
[2] Department of Nuclear Safety Engineering, Nuclear Installations Safety Division, Atomic Energy Authority, Cairo 13759, Egypt
[3] Department of Biology, College of Science and Humanities at Ad-Dawadimi, Shaqra University, Shaqra 11911, Saudi Arabia; mcharni@su.edu.sa
[4] Laboratory of Biodiversity, Parasitology and Ecology of Aquatic Ecosystems LR18ES05, Faculty of Sciences of Tunis, University of Tunis El Manar, Tunis 2092, Tunisia
[5] Department of Chemistry, College of Women for Science, Arts and Education, Ain Shams University, Cairo 11566, Egypt
* Correspondence: hjomaah@su.edu.sa or hassan_emgh@yahoo.com (H.E.G.); fatma_emgh@yahoo.com or fjomaah@su.edu.sa (F.A.G.)

Abstract: Ensuring sustainability of groundwater (GW) resources requires understanding the interplaying factors in the hydrogeochemical evolution of the system (cause and effect relationships), which is the subject of the current work concerning the groundwater resource in a hyperarid region, namely, AdDawadmi, Saudi Arabia. Integration of geographical information system (GIS), statistical, graphical, and geochemical modeling approaches are adopted to achieve the study's design intentions. Slicing the study area on a spatial basis helped yield insights into major constituents' variation trends using the graphical methods that lack spatial representation capabilities, such as Piper, radial, and Durov plots. Localities of higher salinities, NO_3^-, SO_4^{2-}, Cl^-, Na^+, and Ca^{2+} are remarkable, indicating the effects of localized and point source activities and evaporation-driven concentrating processes rather than lithology supported by the largest regression and correlation coefficients for Cl^-, Na^+, and SO_4^2. Many interacting processes are identified: evaporation, vicious salinization cycle (VSC), rock weathering, ion exchange, and geomorphological-driven flow. Hydrogeochemical modeling using the Visual MINTEQ program concludes that concentration-driven evaporation might lead to the precipitation of significant SO_4^{2-} and Ca^{2+} along with $CaCO_3$ saturation. Such processes, coupled with the ion exchange, would greatly impact the GW chemical composition and affect the aquifer and soil properties such as permeability. Human activities impact the GW system, necessitating remediation plans and protection policies to prevent overexploitation and brook the VSC. Finally, the integration of the adopted approaches was found useful, constraining the findings of one approach, reducing the associated uncertainties, enhancing the confidence level and reliability of the obtained conclusions, and obtaining useful information, enabling understanding of the internally interacting processes otherwise hidden.

Keywords: groundwater sustainability; GIS and geostatistical analysis; hyperaridity; geochemical modeling; Visual MINTEQ; Saudi Arabia; vicious salinization cycle; climatic change

Citation: Gomaa, H.E.; Alotibi, A.A.; Charni, M.; Gomaa, F.A. Integrating GIS, Statistical, Hydrogeochemical Modeling and Graphical Approaches for Hydrogeochemical Evaluation of Ad-Dawadmi Ground Water, Saudi Arabia: Status and Implications of Evaporation and Rock–Water Interactions. *Sustainability* **2023**, *15*, 4863. https://doi.org/10.3390/su15064863

Academic Editor: Ozgur Kisi

Received: 26 January 2023
Revised: 16 February 2023
Accepted: 6 March 2023
Published: 9 March 2023

1. Introduction

The Kingdom of Saudi Arabia (KSA) has no surface freshwater resources except for some small temporary wadis. Although its withdrawals were more than 20 billion

cubic meters (BCM) in 2010, it had only 2.4 BCM annual renewable resources. Hence, KSA abstracts more than 80% of its water needs from fossil, non-renewable precious groundwater (GW) reserves. Agricultural, landscape, and livestock activities mostly avail from fossil and renewable GW abstractions. While the domestic and industrial sectors growingly rely upon high-cost and energy-intensive desalination [1–6]. The thirstiest agricultural activities, including livestock ranching and poultry, consume 85% of total GW withdrawal in KSA, a water-stressed arid desert region. This abstraction rate, exceeding that of recharge, is unsustainable, causing rapid depletion, water level decline, and enhanced deterioration, leading to reduced usability and limited quantity that may last less than 50 years [2,7–11]. The quality of GW in KSA's water-stressed hyperarid desert regions, such as AdDawadmi, is likely to be intensely affected by aridity, prolonged drought periods, lithology, hydrogeochemical interactions, and various anthropogenic activities associated with overexploitation, and intensified land use. The KSA ranks third as the largest per capita water user worldwide. It has faced inequality between its input renewable water budget and demands primarily resolved through the overexploitation of fossil GW coupled with desalination for domestic uses and recently reusing treated wastewater [6]. It is, therefore, essential to study and evaluate the GW quality and recognize its type, history, and genesis of mineralization to protect the aquifer from excessive withdrawal, optimize its use, and ensure its sustainability for continuous water extraction.

Water resource explorations and their quality and suitability evaluations are within the highest priorities of the KSA to realize the 2030 vision, which involves a detailed blueprint for preserving the environment and natural resources. Recently, KSA has demonstrated accelerated development, population growth, and living standards. As a result, groundwater (GW) demand has recently been exacerbated due to heavy loadings resulting from irrigation, landscape practices, touristic and sports activities, urbanization, livestock farming, poultry, and population growth. These pressures, coupled with their underfit (unbalanced low and limited precipitation to needs), have led to resource depletion and deterioration [4,5,10,12,13]. In the area under consideration (AdDawadimi metropolitan and its nearby environs), residents entirely rely upon GW since it is the sole source for domestic, industrial, livestock, landscape, tourist, poultry farming, and irrigation purposes. The importance of water geochemical studies is recognizing and understanding the hydrogeochemical and physicochemical processes and factors controlling the groundwater (GW) chemical characteristics. Unfortunately, to our knowledge, there are no data concerning water resources in the AdDawadimi governorate and its nearby environs. Such data are essential for decision makers to involve the area in sustainable development plans. Undoubtedly, natural conditions and anthropogenic activities impact the GW's physicochemical, biological, and quality characteristics. The natural conditions include climatic influences, geomorphology, geology (mineralogy and sedimentology of the containing rocks), and hydrogeological factors. The anthropogenic activities introduce additional stresses related to reclamation, cultivation, urbanization, industrialization, and livestock ranching [14–17]. In GW studies, it is of utmost importance to identify its chemical characteristics, evolution laws, and the main controlling factors and processes. In such studies, the main questions to be resolved include, but are not limited to (1)what are the ultimate sources and sinks of solutes; (2) how does the GW's chemistry evolve; (3) how does the system respond to both natural and anthropogenic activities; (4) what does make it unsuitable for domestic, municipal, or irrigated agriculture uses; and (5) what are the prominent actors on the quality of GW.

Generally, agriculture may cause adverse effects, primarily on shallow aquifers, due to pesticides and organic and chemical fertilizers [18,19]. Other contributors include livestock ranching, which generates a high quantity of animal manure, septic tanks, buried storage tanks, and landfill leachates, bringing a reasonable biological contamination load to the aquifer. Another prominent process that modifies GW's chemistry is the vicious wetting and drying cycle, which is continuous consecutive precipitation and dissolution due to evaporation, especially in arid and hyperarid climatic regions. In such a process, the

concentration of ions having higher solubility grows while those with lower solubility increase to a lesser extent [20–23]. However, the process is not a net source of solutes and involves mainly redistribution of the solutes load within the system, presenting immense stress and salinization mechanisms in prolonged drought periods and limited rainfall during wetting seasons.

When integrated, local spatial statistics and geographical information system (GIS) tools can provide large-scale handling variations [24–26] since the GIS mapping capability provides means of contrasting solutes and parameter distribution with other spatial datasets facilitating visualizing the intercorrelations and interpreting the results. These underpinning tools for geospatial analysis may be extremely valuable for managing groundwater resources to understand GW evolution and demarcate local variations. Researchers have recently widened the application of these techniques in GW-related studies with different objectives and scopes [24,27–32].

In the area under consideration (AdDawadimi governorate and its near environs), residents merely rely on GW since it is the sole water source for irrigation and agriculture, livestock ranching, poultry, domestic, industrial, and landscaping purposes. The area has demonstrated, in recent years, significant urbanization, extension, and population growth. Therefore, it is imperative to delineate the interplaying factors, such as geological formations and anthropogenic activities affecting the precious limited stock of the GW reserve.

The design intention of this study is to integrate GIS, statistical, and graphical approaches to:

(a) Evaluate the hydrogeochemical status and understand the implications of evaporation, rock–water interactions, and the interplaying factors;
(b) Identify the GW chemistry's hydrogeochemical characteristics in the AdDawadimi governorate and its nearby environs, Riyadh region, Saudi Arabia.

Integration of all such approaches is anticipated to help understand the effects of hyper-aridity, intensive agricultural activities, and higher daylight temperatures and define their deteriorating stresses on the quality of the GW reserve in the region. To help reduce the spatial distribution-related limitations of the well-established plots, such as Piper, radial, and Durov plots, the study area was sliced into portions for demarcating variations among localities instead of their application to the whole studied area. The hydrogeochemical modeling program, Visual MINTEQ, was used to demarcate whether the GW system is oversaturated, undersaturated, or at equilibrium. Integration of many different approaches is the adopted strategy to elucidate otherwise hidden phenomena and distributions constraining the findings of one approach. Moreover, a statistical analysis is presented to help mark the correlation between the different affecting factors. The ultimate goal of this work is to evaluate and assess the interplaying hydrogeochemical processes affecting and controlling the evolution of the GW system. This is essential for decision makers to involve the area in sustainable development plans. Despite the utmost importance of these studies, which could provide indistinguishable information to decision makers and policy planners, they are very scarce in the AdDawadimi governorate, and we could not find one such study specific to the region. To our knowledge, this work represents the first-of-a-kind water resource quality study on the region under consideration.

1.1. The Study Area

1.1.1. Location, Physiography, and Climate

AdDawadmi governorate lies northwest of Riyadh Province, Saudi Arabia, with its western half at the outermost eastern fringe of the so-called Arabian Shield. The governorate surface is mostly flat, with numerous rocky outcrops and plateaus. The governorate morphology generally slopes towards the east and northeast with a mean elevation of 940 m above mean sea level (AMSL). The Jabal Al-Nir in the far west is the highest at 1307 m, and the far northeast is the lowest plain at 660, see Figure 1. The shallow sedimentary thickness ranges from 1.0 to 7.0 m, overlying the bedrock, and generally slopes

from the west to the east [33]. The governorate's surface abounds with huge mountains, plateaus, sand dunes, and valleys. Many large and small wadis, large valleys, small reefs, and valleys are distributed throughout the study area, such as Al-Rasha valley, Wadi Khnuqa, wadi Abu Ashland, and Shoaib Dawadmi. The Ad-Dawadmi is famous for cultivating diverse crops and has witnessed salient agricultural outgrowth in the past thirty years, yet has been providential in preserving its production levels.

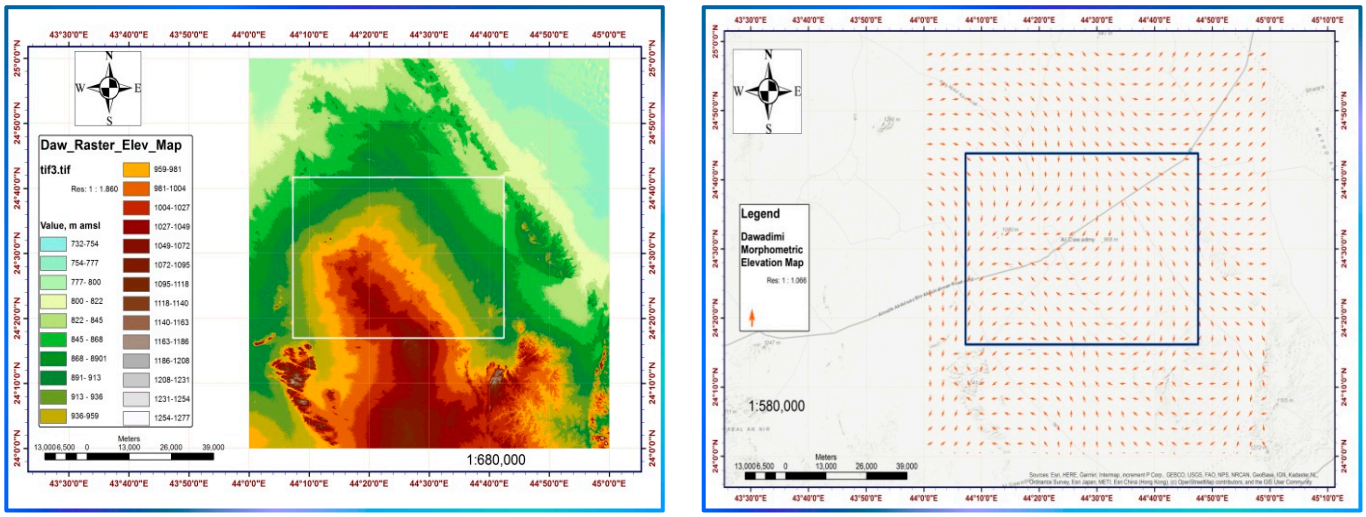

(**a**) (**b**)

Figure 1. A digital elevation model of the study area (**a**), and its vectorized representation (**b**) of the AdDawadmi governorate, Saudi Arabia.

Moreover, pasture-based livestock farming (primarily camels, goats, and sheep), poultry farms, and aquaculture are widely spread [9,34]. The climate of the Ad-Dawadmi governorate is ordinarily hyper-arid. The precipitation is limited, intermittent, and recently affected by climatic change with long consecutive drought periods; the last rainy season was in 2017, with subsequent limited occasional shower storms. From 2005 to 2015, the long-term yearly average is only 4.9 mm, with an average temperature of 8 °C for cold periods and 42 °C for the hot season [35].

1.1.2. Geological Settings

AdDawadmi lies at the Arabian Shield eastern-central border with unconformably overlying Palaeozoic sediments in the central KSA high-pediment-containing Precambrian granitic rocks complex coupled to two belts of folded metasediments and two oval layered basic complexes [36]. Those metasediments comprise sulfide and silver mineralization localized in parts of an extensive fracture N–S trending belt across the territory. The conformable calcareous Ar-Ridaniyah, arenaceous, and semipelitic Abt formations are the oldest rocks deposited in a transgressive subsiding likely marine environment during the Precambrian, Figure 2. The AdDawadmi governorate is considered to contain the following four main geologic units [36–38]: A granitic batholith makes up over 80% of the district and constitutes three granitic varieties. Two-layered basic intrusions occur in the district, a southern one, AlJe'alani, an area of about 50 km^2, and a northern one, Arja, covering 9 km^2. Both are oval and contain inwardly dipping igneous layers. In the north and the southeast, metamorphic sedimentary successions occur; these are unconformably overlain in the east by Ordovician sandstone. A well-developed fracture pattern characterizes the district where swarms of dykes and zinc–lead–silver veins have intruded. The metasediments belong to two conformable formations, the lower Ar-Ridaniyah, which constitutes a quartz-feldspathic unit at the base, and an overlying Abt, which is essentially pelitic and semi-pelitic. The district represents the Najd orogeny by the emplacement of post-kinematic

granitic intrusions with extensive secondary fracturing partly emplaced by zinc–lead–silver veins and subsequent dyke intrusion.

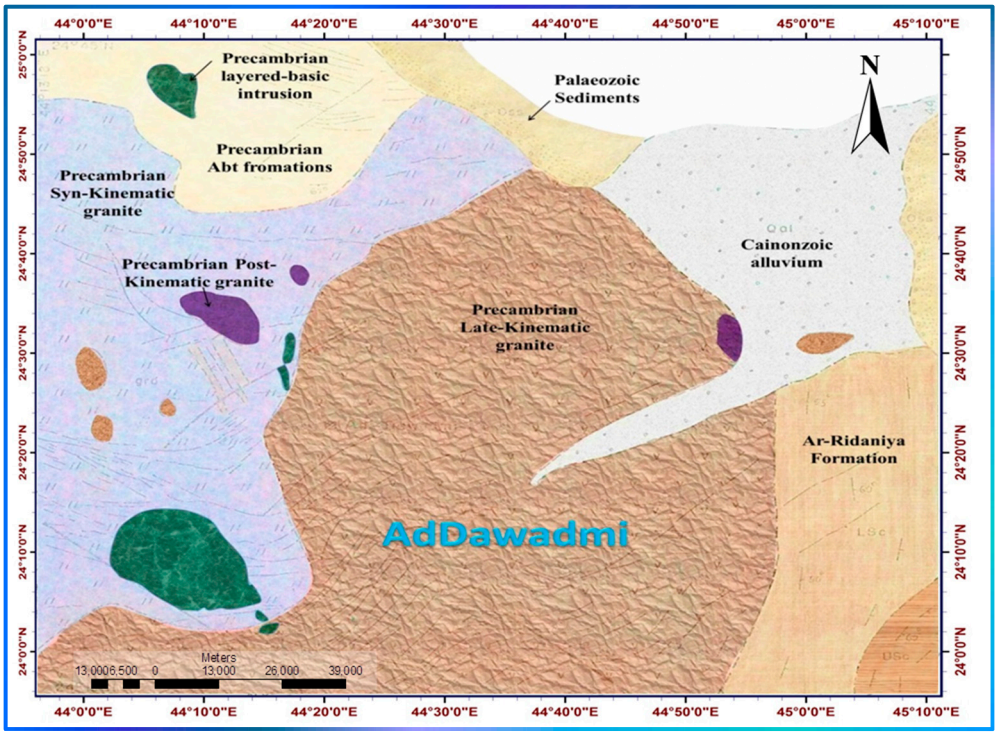

Figure 2. Simplified geological map of the AdDawadmi Governorate; redrawn after [37].

Deformations and the subsequent metamorphism to greenschist facies were due to ultrabasic and basic rock intrusions. Detailed studies on Al-Jealani intrusion have indicated the formation of layered gabbroic rocks with persistent dominant plagioclase and the strong amphibolitization of the units rich in pyroxene. The metals initially present in the N–S trending belt of preexisting sedimentary rocks are thought to have been mobilized, concentrated, and deposited by the medium of hydrothermal fluids related to post-kinematic granitic activity during the last orogenic episode. The ore minerals within the fractures are sphalerite, galena, native silver, silver sulfosalts, and sulfides. The other genetic type is an iron–zinc sulfide deposit in the form of metamorphosed and structurally disrupted strata-bound lenses within the calcareous horizon of the Ar-Ridaniyah formation. In a sedimentary calcareous environment, the pyrrhotite and sphalerite are mineralized as metamorphosed syngenetic–diagenetic [37–39].

Groundwater, the artery of life ecologically and sustainably, is the sole available water resource since precipitation is very limited in duration and, recently, in amount. However, characterizing, monitoring, and studying the cause-and-effect relationship for the aquifer in the region are scarce or have not been conducted at all [34]. Hence, the hydrological characteristics of the study region such as types, numbers, reserves estimates, thicknesses of the aquifer/s, hydraulic conductivity, transmissivity, specific yield, etc.) are all missing since this is a first-of-a-kind study in such an area. The study region is the central part of the district, namely, the AdDawadmi metropolitan and its nearby environs (latitudes 24°20′ to 24°40′ N and longitudes 44°12′ to 44°33′ E). The water table levels were consistently in the range of a few meters, 2–3, and even less below ground level (BGL) in 1996 [33]. These levels have declined very sharply and are consistently more than 12 m BGL. The asymptotic spatial distribution natural neighbor interpolated piezometric levels map is given in Figure 3, ascertaining that the piezometric level follows the general slope trend from west to east and northeast.

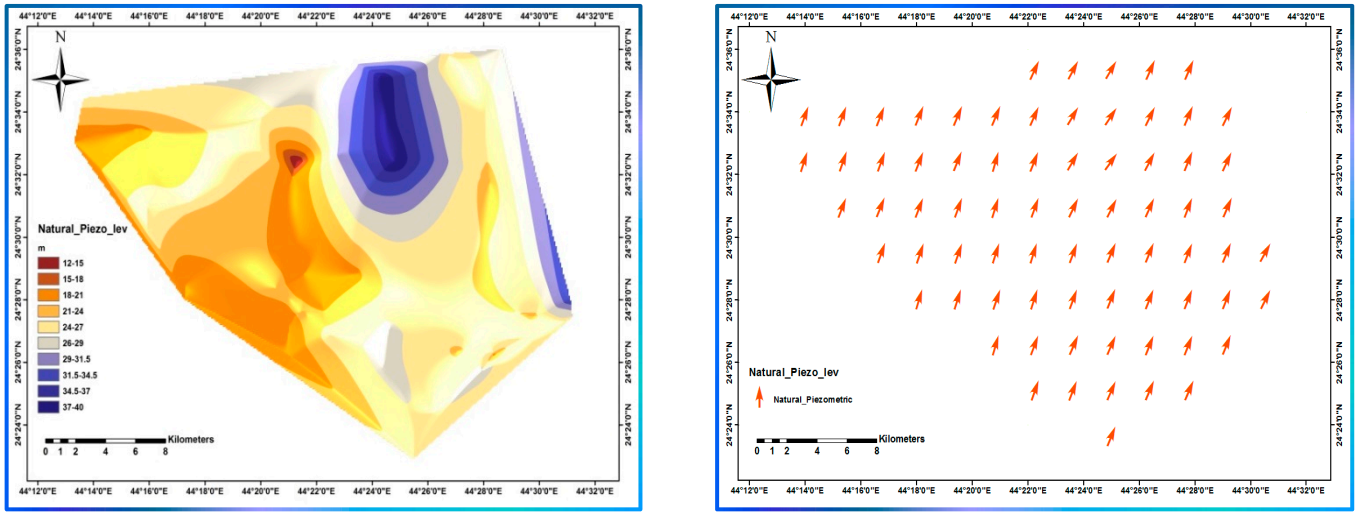

(**a**) (**b**)

Figure 3. Natural neighbor interpolated piezometric level: (**a**): classified; (**b**): vectorized.

2. Materials and Methods

2.1. Sampling and Preservation

Forty-seven GW samples were collected from the accessible and active wells. Before the sample collection, representative aquifers' water was attained by pumping enough to reflect the well's water geochemistry with the least possible uncertainty. Plastic bottles of 1 L volume were thoroughly rinsed several times with the well water before being filled, preserved, and cooled according to the measurand(s) precautions and rules. Samples collected for the hydrochemical analyses received no preservatives; upon going back to the Water and Environment Research Unit, College of Science and Humanities at Ad-Dawadmi, Shaqra University laboratory (WERU), samples were split, pretreated, and acidified to pH < 2 (for analysis of NO_3^- and NH_4^+) according to the standard methods and sampling directions [40,41]. The areal distribution of the sampling points' locations is in Figure 4.

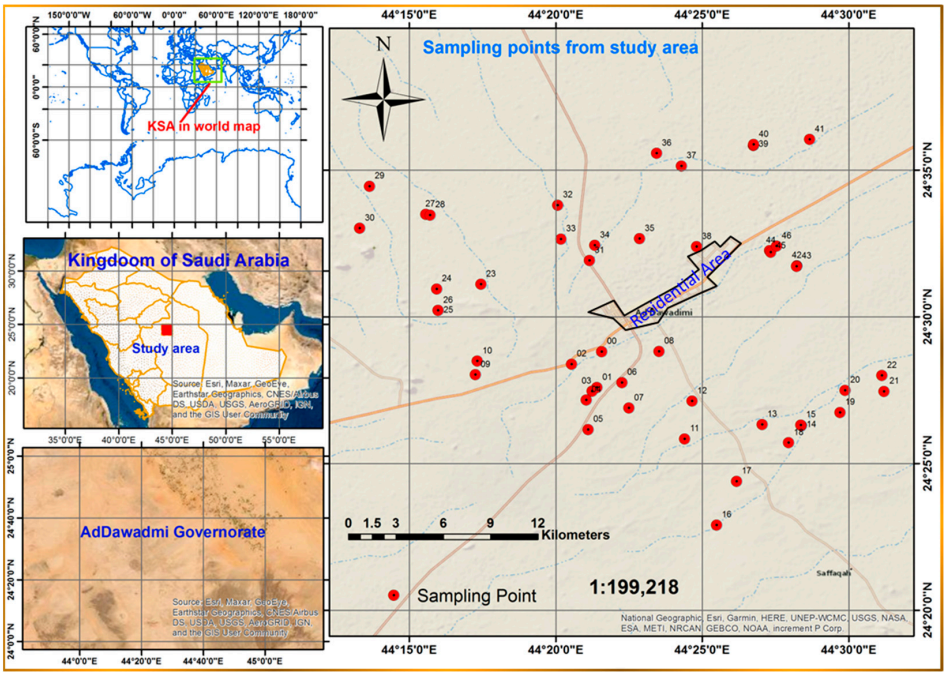

Figure 4. The areal distribution of the sampling points' locations.

2.2. Analyses and Procedures

The electrical conductivity (EC), pH, temperature, and dissolved oxygen (DO) parameters were measured immediately in-field using ThermoScientifiфc (Waltham, MA, USA), ORION STAR A122 electrical conductivity meter, PascoScientific (Roseville, CA, USA) pH electrode connected to an Explorer GLX, Pasco data logger via PASPort CHEMISTRY Sensor, PascoScientific, independent temperature electrode connected through the Passport CHEMISTRY Sensor, and, Pasco Scientific DO electrode, respectively. All meters were calibrated, stored, and maintained per the manufacturer's instructions.

2.3. Hydrochemical Characterization

When conducting an analytical method, three separate considerations of experimental error are usually made (i.e., before an analysis, during the analysis, and at the end of the analysis). Errors known or believed to affect the result should be minimized as practically as possible via, for example, monitoring the measurement process and evaluating the quality of the measurements and their fit to the original study design criteria. Method validation evaluates whether the precision and accuracy obtained by following the procedure are appropriate for the problem (results are fit-for-purpose). Before a procedure can provide useful analytical information, it must demonstrate that it can provide acceptable and reliable results. Usually, validation uses a standard sample whose composition closely matches the samples to which the procedure must be applied. The procedure's precision was evaluated by comparison of replicate analyses. The current work followed the validated procedures stated in the Standard Methods for examining Water and Wastewater [42]. The standard methods received great validation practices and contained, in some cases, numerous stages to remove interferences and ensure the reliability of the individual result obtained. Relieving some of such precautions and preparatory steps may be beneficial as commensurate with the study intentions and required levels of confidence and accuracy.

When such relieving's or modifications were adopted, the rule of thumb that it must not compromise the analysis reliability was assured by applying the respective quality control, operational checks, and quality assurance practices. Bicarbonate (HCO_3^-) is determined titrimetrically against sulfuric acid by neutralization method, APHA procedure No. 2320B, with no pretreatments or filtration and keeping the sample out of contact with air. Chloride (Cl^-) was determined trigonometrically against silver nitrate (APHA procedure No.4500-B Cl^-) using a potassium chromate indicator. Complexometric titration using disodium EDTA was used in determining Ca^{2+} and Mg^{2+} [43]. A flame photometer (MICROPROCESSOR FlamePhotometer, Model-1382, Electronics India, India) measured Na^+ and K^+ concentrations following APHA procedures No.3500-Na B and 3500-K B. The turbidimetric method (procedure No.4500-SO_4^{2-} E) was followed to measure sulfate (SO_4^{2-}) ion concentration using JENWAY 6850 UV/Vis. Spectrophotometer at 420 nm wavelength (Jenway, London, UK).

Nitrate (NO_3^-) ion concentration was quantified spectrophotometrically at 410 nm wavelength following the modified phenol sulfonic acid method [44], which received further refinement and tuning to yield an intense and stable colored complex. The addition of 25 mL of 6N NH_4OH instead of the initially devised 3N in the complexing step yielded stable, intense, and reproducible color intensity. The accuracy and precision of the tuned procedure were evaluated, assuring the modification validity, robustness, and purpose-fitness. The modified ammonia diffusion method [45] was followed to collect and concentrate the dissolved NH_4^+ ion. The collected NH_4^+ was quantified spectrophotometrically following Nessler's method at 405 nm wavelength. Dissolved organic carbon (DOC) was estimated spectrophotometrically at 254 nm wavelength using potassium hydrogen phthalate (PHP) as a proxy, yielding R^2 consistently higher than 0.99 [45].

2.4. Statistical Analyses

The statistical analysis of hydrogeochemical data has become common and indispensable in recent years with different degrees of complexity. This practice finds good opportunities

due to user-friendly software, which dramatically automates and facilitates execution. In addition, statistical analyses have been found to provide fruitful insights and views for the data at hand and help mine the implicit relationships and mutual effects that can be very helpful in delineating the controlling factors of system chemistry. Descriptive statistics, regression analysis, and Spearman rho correlation coefficient tests were executed to highlight and figure out the significant relations between the individual constituents [46–51]. Different statistical analyses and representations were executed using the Minitab@18 statistical package. The methods applied and representations will be hinted at, explained, and commented on in their respective sections.

2.5. Geospatial and Geostatistical Analyses

ArcGIS 10.8 software spatial analysis tools were employed to analyze, map, interpolate, aggregate, and represent the GW hydrological and physicochemical data. Geostatistical analysis methods were used to study the spatial distribution of the interpolated concerning parameters and solutes variation in space. The Inverse distance weighted (IDW) interpolation method was adopted since it applied less smoothening algorithms that keep visualizing the local variation with a better spatial resolution [30]. IDW interpolation algorithm determines cell values using a linearly weighted combination of a set of sample points, with the weight being a function of the inverse distance [52].

2.6. Analysis of the Hydrogeochemical Water Quality

AquaChem®10 Water Quality Data Analysis and Reporting Software. It comprises analysis tools that cover a range of functions, calculations, and robust analytical capabilities complemented by a selection of commonly used geochemical plots, such as Piper, Schoeller, Ludwig–Langelier, Durov, scatter plots, and Wilcox, to represent and conclude the chemical features. It is widely employed to classify, analyze, plot, and report hydrogeochemical and biogeochemical data.

3. Results and Discussion

3.1. Water Quality Characterization

The descriptive statistics summary of the physicochemical and field characteristics for the collected GW samples is given in Table 1. The information indicated that they were semi-neutral to slightly alkaline (pHs range from 6.8 to 8.35) with 7.33 on average and standard deviation (stdev) of ±0.35, n = 47. The GW pH plays a significant role in the geochemical equilibrium, especially dissolution/precipitation processes, so it is considered an essential parameter to measure [53]. Electrical conductivities (ECs) varied significantly, spanning over 255 to 17,990 µS/cm with a similar divergent range of TDS calculated as 0.65 fractions of ECs. The samples' temperatures were from 21 to 31.9 °C, with an average of 27.32 °C, stdev of ±2.17, n = 47. The GW temperature variations are linked to the recharge with rainfall; relatively higher temperatures are seen for deep GW, and the reverse is for shallow GW [54]. Although temperature and pH are not water health-related parameters under direct regulation, they represent the independent and uncontrollable geochemical equilibrium state governors.

The ionic charge balance equilibrium (ICBE) among total cations (TZ^+) and total anions (TZ^-) was found to be within ±10%, ranging from −9.79 to +6.84, with mean and median values of −2.46 and −3.45, respectively, and stdev of ±4.48. The Anderson–Darling normality test revealed that CBE is normally distributed with a p-value < 0.036. Although skewness and Kurtosis indicated a mild shift towards the negative wing, such statistics still reveal that the entire analyses are under statistical control providing fit-for-purpose confidence in the acceptability and reliability of the analytical data. The reason behind this ICBE widening is the immense divergent ECs. The cations content of Na^+, K^+, Ca^{2+}, and Mg^{2+} in all GW samples exhibited the ranges of 10.7–2380, 1.52–19.6, 41.7–1668.2, and 0.5–670.5 mg/L, respectively. While the anions content of HCO_3^-, Cl^-, SO_4^{2-}, and NO_3^- occupied the ranges of 128.9–536, 19–5074, 13–3322, and 0.21–269.28 mg/L, respectively. All

constituents spanned over many orders of magnitude except for that of HCO_3^-. HCO_3^- was changed over a relatively limited range compared to all other constituents. Figure 5 shows the box plot of the examined major constituents and physical parameters distribution. As evident from Figure 5, most parameters are not normally distributed, pointing out localized acting processes or point sources representing an accumulation function in the groundwater system under consideration.

Table 1. Descriptive Statistics summary of the measured and collected Physicochemical properties.

Variable	Mean	Median	SE Mean	SD	Coef. Var	Min	Q1	Q3	Max.	Range	IQR	Skewness	Kurtosis
pH	7.3372	7.3300	0.0504	0.3454	4.71	6.8000	7.1000	7.5400	8.3500	1.5500	0.4400	0.64	0.37
Temp., °C	27.321	27.500	0.316	2.168	7.94	21.500	25.000	29.000	31.800	10.300	4.000	−0.10	−0.13
DO, mg/L	11.877	12.400	0.275	1.882	15.85	7.000	10.400	13.200	14.500	7.500	2.800	−0.78	−0.22
Odor	0.00426	0.00000	0.00426	0.02917	685.57	0.00000	0.0000	0.00000	0.20000	0.20000	0.00000	6.86	47.00
Appearance	0.1340	0.0000	0.0469	0.3212	239.62	0.0000	0.0000	0.0000	1.0000	1.0000	0.0000	2.23	3.45
Alt., m amsl	976.23	985.00	4.17	28.60	2.93	911.00	947.00	996.00	1034.00	123.00	49.00	−0.37	−0.71
DWL, m bgl	23.979	25.000	0.770	5.277	22.01	12.000	20.000	26.000	40.000	28.000	6.000	0.92	2.42
WD, m bgl	38.43	40.00	1.21	8.28	21.54	25.00	30.00	45.00	52.00	27.00	15.00	0.03	−1.09
Disch., m^3/d	37.77	40.00	2.31	15.84	41.94	15.00	30.00	40.00	80.00	65.00	10.00	0.81	0.51
EC, µS/cm	5227	4280	546	3745	71.65	255	2939	7050	17,990	17,735	4111	1.39	2.18
TDS, mg/L	3293	2696	344	2359	71.65	161	1852	4442	11,334	11,173	2590	1.39	2.18
Na^+ mg/L	661.8	504.0	84.6	580.0	87.64	10.7	260.0	801.0	2380.0	2369.3	541.0	1.38	1.08
K^+ mg/L	6.607	5.700	0.563	3.861	58.43	1.520	3.800	8.600	19.600	18.080	4.800	1.30	1.98
Ca^{2+} mg/L	518.0	433.7	54.9	376.1	72.61	41.7	229.4	698.5	1668.2	1626.5	469.2	1.18	1.31
Mg^{2+} mg/L	84.3	60.7	15.1	103.8	123.16	0.5	22.8	126.5	670.5	670.0	103.7	4.12	22.24
NH_4^+ mg/L	0.02	0.01	0.01	0.04	150.10	0.00	0.00	0.04	0.18	0.18	0.04	2.44	7.49
HCO_3^- mg/L	314.9	302.6	15.0	102.8	32.65	128.9	242.1	374.4	536.0	407.1	132.3	0.30	−0.54
Cl^- mg/L	1038	660	150	1028	98.96	19	343	1518	5074	5055	1175	1.78	3.95
SO_4^{2-} mg/L	1303	1163	121	830	63.72	13	644	1980	3322	3309	1336	0.57	−0.31
NO_3^- mg/L	72.70	51.24	9.87	67.67	93.09	0.21	28.94	116.53	269.28	269.07	87.59	1.48	1.80
TC, epm	61.84	51.71	6.58	45.10	72.92	3.02	29.42	91.74	208.39	205.37	62.32	1.14	1.22
TA, epm	62.72	52.82	6.30	43.21	68.90	3.49	33.06	84.03	196.01	192.51	50.97	1.09	1.03
ICBE, %	−2.462	−3.449	0.653	4.479	−181.94	−9.799	−6.046	0.313	6.842	16.642	6.359	0.43	−0.84
DOC, mg/L	1.893	1.477	0.208	1.425	75.28	0.134	0.893	2.550	7.651	7.517	1.658	1.82	4.80

DO: dissolved oxygen; Alt.: Altitude; ams: Above mean sea level; DWL: depth to water level; bgl: below ground level; WD: well depth; Disch: well discharge; EC: electrical conductivity; TDS: total dissolved solids; TC: total cations; TA: total anions; ICBE: Ionic charge balance equilibrium; DOC: dissolved organic carbon; epm: equivalents per million, m3/d: cubic meter per day.

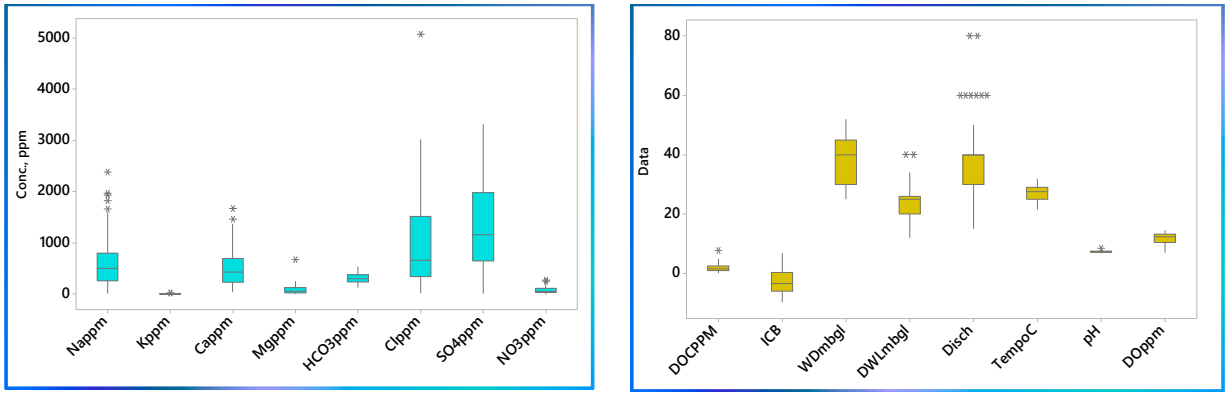

(**a**) (**b**)

Figure 5. Box plot the major constituents (**a**) and physical parameters distribution (**b**).

3.2. Major Constituents Analysis

Generally, Cl^-, SO_4^{2-}, Na^+, and Ca^{2+} are mutually the most predominant anions and cations of the major constituents. The study area was partitioned into different portions on an areal basis, namely, north, south, east, west, northeast, southeast, northwest, and southwest. The average distribution of major constituents throughout those sections is shown in the radial diagram in Figure 6. The distributions indicated that the relative proportions are quasi-uniform throughout the area, whatever the section is. However, the total load exhibited a recognized spatial variation, with the most loads appearing in the northern half and especially the northeastern section, following the general geomorphological trend

in Figure 1. The spatial variations among individual constituents are not remarkable, indicating that this might be due to a relatively common acting process (i.e., a process affecting the major constituents to a comparable extent). The most probable concentrating processes are rock weathering and evaporation. The rock weathering process necessitates the geological settings to be the same throughout the study area, which is not the case, as evidenced in Figure 1. The other process, anthropogenic-driven evaporation, remains the possible mechanism leading to the observed salinization, provided that differences in the rates of such process effects the observed dissimilarities and spatial variations. However, there is no information or even observation to support this hypothesis. The authors claim that the net effect observed might be ascribed to both processes with a contribution from a third one leading to the pronounced variation in the northern part, which is thought to be the geomorphological-driven flow of higher saltwater (i.e., the uppermost layer of water infiltrated through the soil with much-solubilized contents of soil salts) from south to north. Such a claim will be further investigated in the following sections.

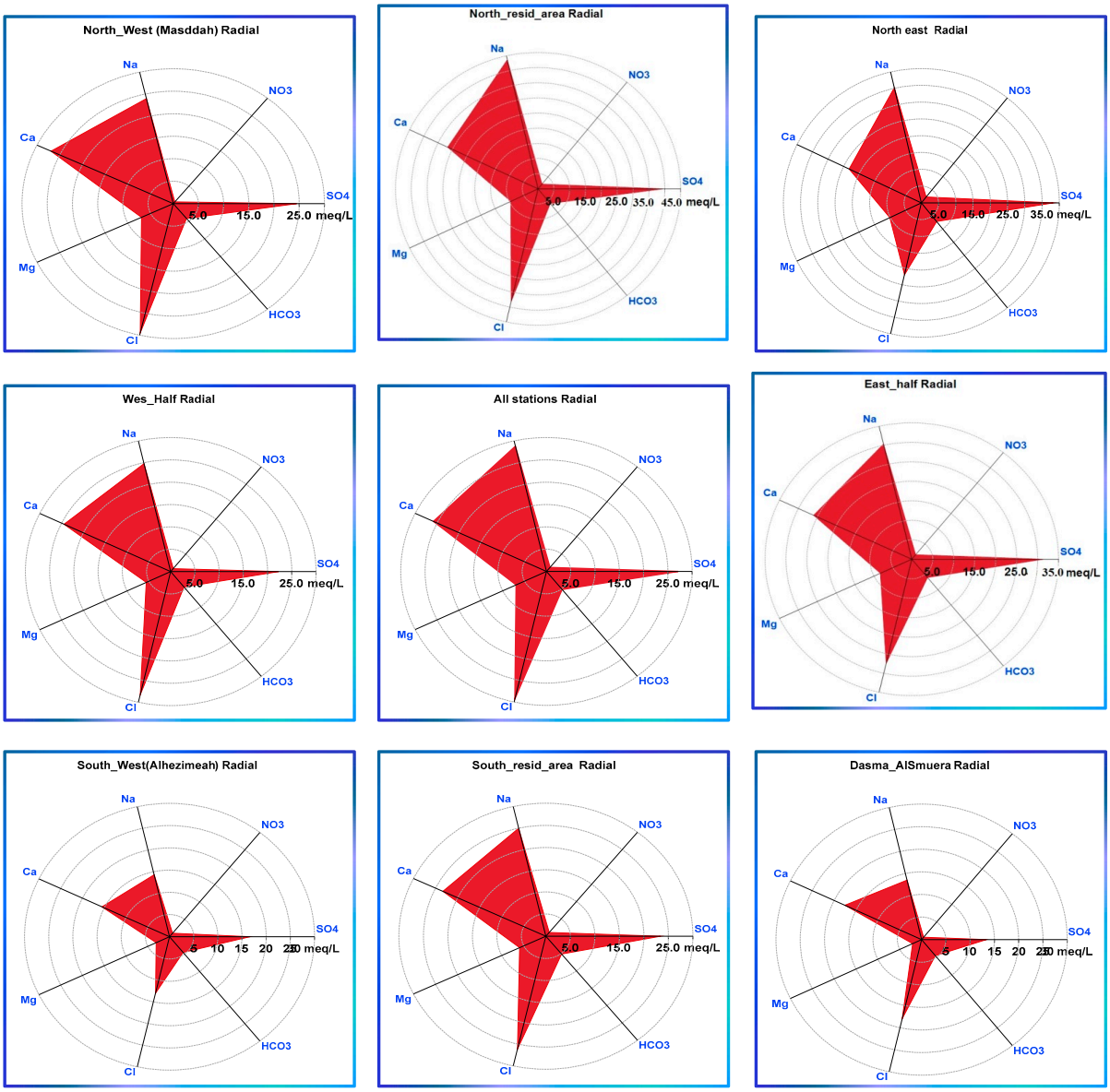

Figure 6. Radial distribution of the major constituents throughout the study area on a spatially sectionalized basis.

3.3. Classification of Groundwater Using Geochemical Diagrams

Over the last decades, many hydrochemical diagrams have been developed and applied with diverse aims to understand better the GW system's interpretation, particularly, the GW system's controlling processes, hydrogeochemical facies, and its evolutionary trends. Of those diagrams, the Chadha [55], the Piper [56], the Durov, Schoeller, scatter (ion ratios), Pie, and Ludwig–Langeiler plots are invoked and utilized in the following section.

3.3.1. Chadha Plot

The occurrence modes of GW in reservoirs that differ in their chemical composition are described as hydrogeochemical facies. Many plots provide comparable and/or synonymous information regarding hydrochemical facies such as Chadha, Piper, and Durov. The differences between the alkaline earth and alkali metals in the Chadha plot are plotted on the abscissa expressed as percent reacting milliequivalents. While on the ordinate axis, the differences between weak acidic and strong acidic anions are plotted by the same units as those used in the x-axis. The Chadha plot of GW samples from the study area is shown in Figure 7. Figure 7 shows that 61.73% of the total samples fall under the subfield of alkaline earth exceeding alkali metals and strong acidic anions exceeding weak acidic (Ca^{2+}-Mg^{2+}-Cl^{-}) water type with a permanent hardness category. About one-fifth of the GW samples fall under the Na^{+}-Cl^{-} subfield, namely, 21.27%, which poses salinity problems in irrigation, livestock farming, and domestic and industrial uses, and 10.63% fall under the subfield that strong acidic anions exceed weak acidic anions. The remaining minor fractions, 4.25 and 2.12, fall under the alkaline earth metals exceed alkali metals, and weak acidic ones exceed strong acidic anions subfields, respectively.

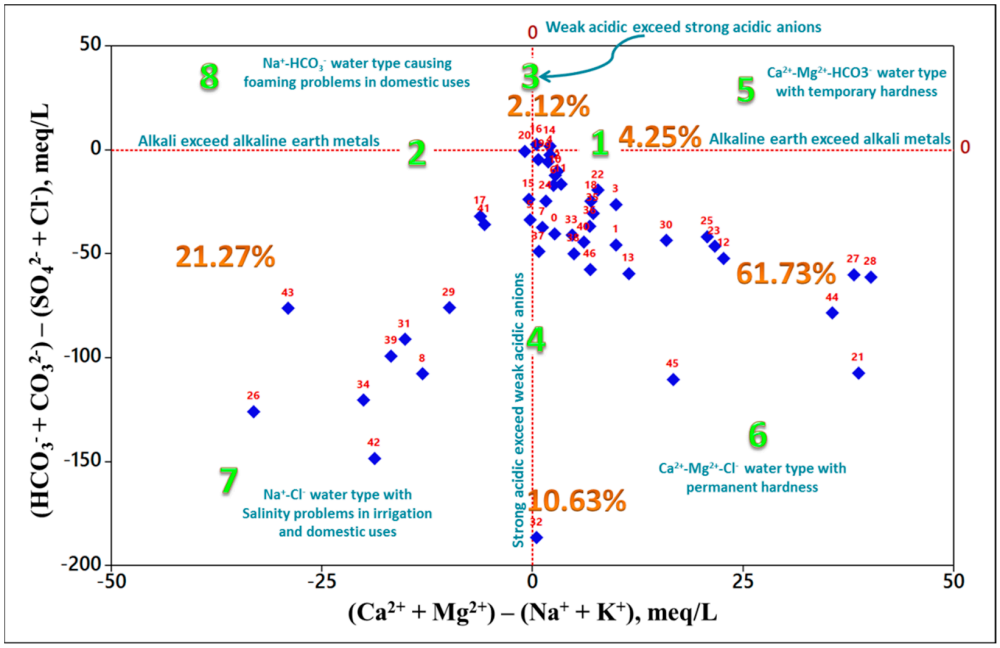

Figure 7. Chadha hydrogeochemical classification.

3.3.2. Piper Plot

The Piper diagram portrays the relative concentrations of the major cations and anions on two trilinear plots, together with a central quadrilateral diamond plot where the points from the two trilinear plots are projected, showing the overall chemical character of the water as milliequivalents percentages [57]. Three data points represent every sample, one in each triangle and one in the projection diamond grid, revealing certain useful properties of the total ion relationships. The Piper plot allows comparisons of six parameters in many samples but does not portray the absolute ion concentrations with relative percentages like

all trilinear plots. The Piper plot's main purpose is to show samples' clustering and infer their hydrogeochemical facies.

The hydrogeochemical properties of GW are a function of the soil texture, aquifer lithology, GW residence time, geology, and water regional flow pattern, hence illustrating the GW's origin, chemical composition, and water types according to the ionic composition [58,59]. The hydrochemical facies delineate GW's chemical composition and demarcate the origin, mixing water from different sources, evolution pathways, and chemical water types [57,60]. A Piper diagram is a widely utilized graphical form that illustrates the general distribution of anions and cations. As a countermeasure for this limitation, the study area was partitioned or sliced into small portions on a spatial basis to look for the localized variabilities from place to place. Figure 8A shows the water quality classifications within a Piper plot, and Figure 8B–J show the Piper plots for all GW in the whole and sliced partitions of the study area, respectively. The main shortcoming of the Piper plot is its inability to demarcate or represent spatial variability. Again, the Piper plot does not portray the absolute ion concentrations but rather the relative percentage like all trilinear plots. So, only the changes in the relative proportions of the major constituents are caught but not the changes in the total load. The diagrams showed no dramatic evolutions of the hydrochemical facies throughout the study area but rather a mild transformation of the relative proportions from one locality to another with no definite regime (i.e., the data are broadly distributed rather than forming distinct clusters). Such a theme may suggest the presence of a relatively similar water–rock interaction regime, and the anthropogenic activities all over the area under consideration that did not alter the relative chemical composition. The samples generally lie in the Cl^- and SO_4^{2-} anions dominance fields and Ca^{2+} and Na^+ cations dominance fields. According to the water classification scheme in Figure 8A, samples are distributed descendingly under L, N, and P, respectively, with only one sample falling under each M and O field; i.e., samples fall under Ca^{2+}-Na^+-Cl^--SO_4^{2-} water types. The distribution of samples in the sliced partitions exhibits a somewhat similar theme, especially in the half partitions.

However, for smaller partitions such as northeastern and northwestern, the clustering (narrowing distribution) is apparent, suggesting the presence of homogenous controlling factors acting in the locality. However, the sample distribution in the AdDasma-AsSumera (southeastern, Figure 8J) partition is very broad compared to the size of the locality, with other partitions demarcating dramatic differences within the locality. These dramatic differences may be attributed to different anthropogenic activities within the partition since some wells are far from agricultural and livestock farms and are used mainly for domestic and drinking purposes with apparently reduced TDS levels, while others are within recent farms and the rest are with old farms with far higher levels of TDS, >10,000 mg/L. The cations are distributed in the no dominant, Ca^{2+} dominant, and $Na^+ + K^+$ dominant water types, and the anionic species are distributed within the dominant Cl^-, SO_4^{2-}, and no dominant types, with one sample falling within the HCO_3^- dominant zone. A detailed analysis shows the samples fall under a variety of water types, including Cl^--SO_4^{2-}, $Ca^{2+}(Mg^{2+})$ Cl^- (SO_4^{2-}), $Na^+(K^+)$ $Cl^-(SO_4^{2-})$, and only one sample in $Ca^{2+}(Mg^{2+})$ HCO_3^- water types. Unfortunately, this diagram provides little information to discriminate the separate clusters of samples, which agrees with the comment of Güler et al. [60]. As shown in the central quadrilateral diamond plot, the GW samples mostly fall under the SO_4^{2-}-Cl^- and Ca^{2+}-Mg^{2+} (permanent hardness) parts of calcium chloride-type (non-carbonate hardness), and in the field of SO_4^{2-}-Cl^-, and Na^+–K^+ (saline) of sodium chloride-type (non-carbonate alkali). Only one sample falls under HCO_3^--CO_3^{2-} and Ca^{2+}-Mg^{2+} (temporary hardness), indicating the dissolution of rock-forming minerals such as gypsum, anhydrite, Na-rich rocks, and halite dissolution. In general, samples falling in Na-Cl facies in the diamond field of Piper show a saline nature in the groundwater [61]. These results are consistent with the computed mean values of the mineral phase saturation indices (SIs) that show undersaturation of halite, gypsum, epsomite, and anhydrite and oversaturation of calcite, dolomite, and aragonite.

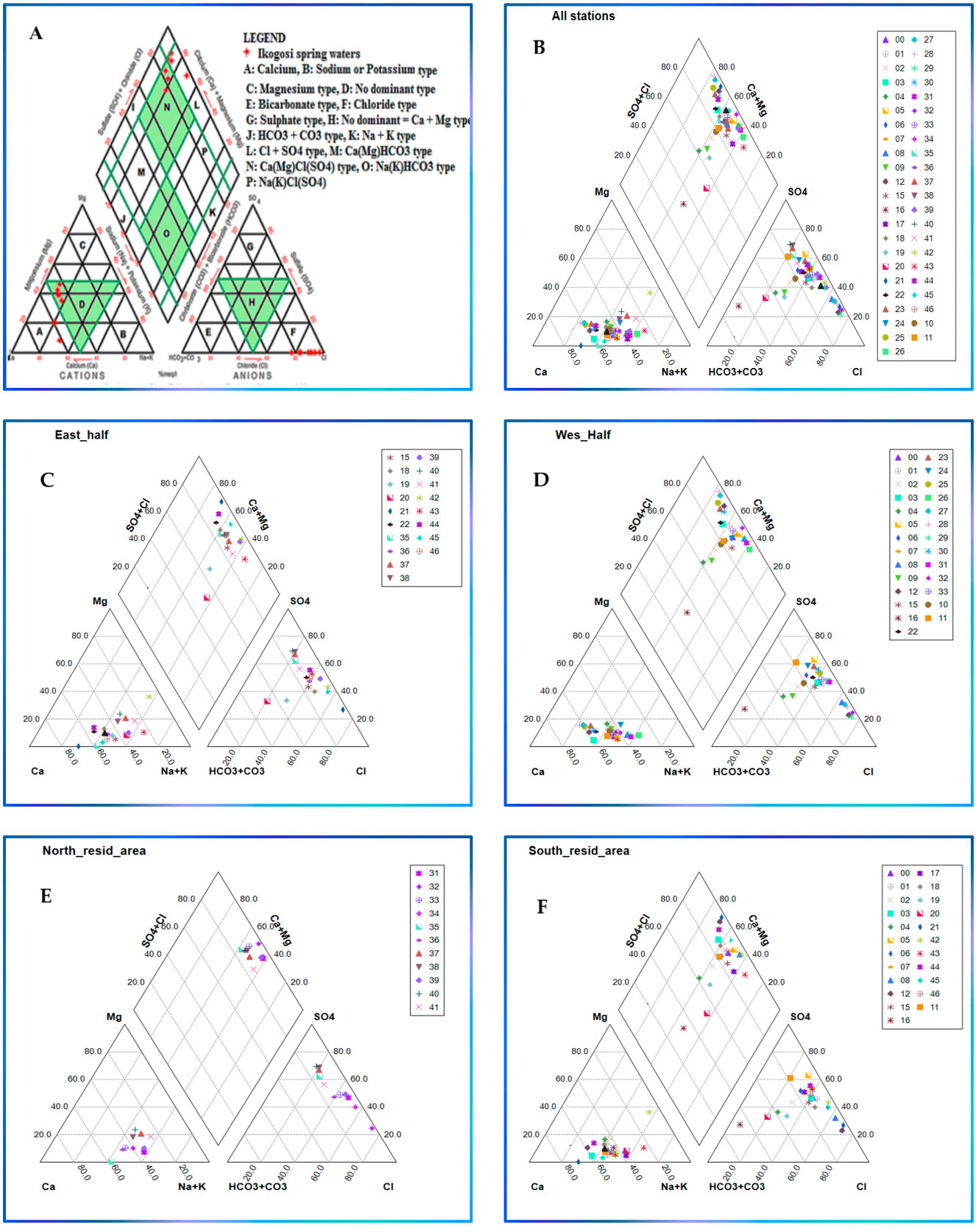

Figure 8. *Cont.*

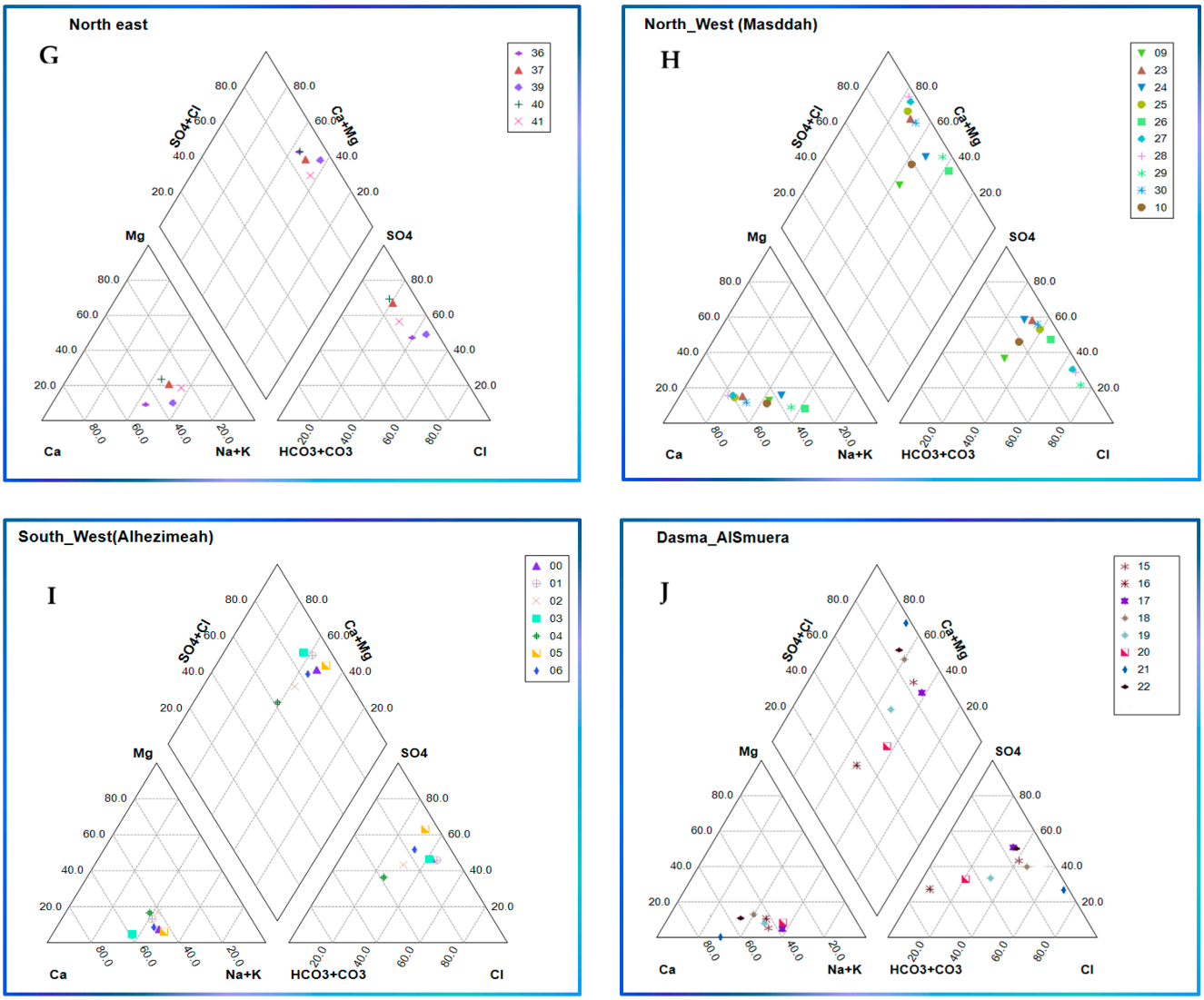

Figure 8. Piper diagram clustering the GW samples of the sliced partitions of the study area: (**A**) shows the meaning of the plot's different sections; (**B**) the plot of the whole study area; (**C**) the Eastern half of the study area; (**D**) Western half of the study area; (**E**) Northern part to the residence area; (**F**) Southern part to the residential area; (**G**) Northeast of the study area; (**H**) Northwest of the study area; (**I**) Southwest of the study area; (**J**) Southeast of the study area (Dasma village).

3.3.3. Schoeller Diagram and Ludwig–Langelier Plot

Schoeller diagram, Figure 9 exhibits a similar theme that shows a high level of Ca^{2+}, Na^{+}, Cl^{-}, and $SO_4{}^{2-}$ and a lower level of Mg^{2+} and $HCO_3{}^{-}$. Generally, strong acids (Cl^{-} and $SO_4{}^{2-}$) are dominant over weak acids ($CO_3{}^{2-}$ and $HCO_3{}^{-}$), whereas alkali metals Na^{+} and K^{+} and alkaline earth metals (Ca^{2+} and Mg^{2+}) are interchangeably comparable. Moreover, Cl^{-} and $SO_4{}^{2-}$ are far higher than Na^{+} or Ca^{2+}, 3.5-1.4:1, as shown in the Ludwig–Langelier plot in Figure 10 and the Pie plot in Figure 11. The GW samples were dominated by the combination of sodium-chloride and calcium-sulfate-type as shown in ion ratios plots in Figure 12 and the Pie plot of the major constituents showing approximately equal proportions of Cl^{-}, Na^{+}, $SO_4{}^{2-}$, and Ca^{2+}, respectively. The bicarbonate anion and magnesium cation were depleted relative to other constituents except in very few samples exhibiting low salinity levels.

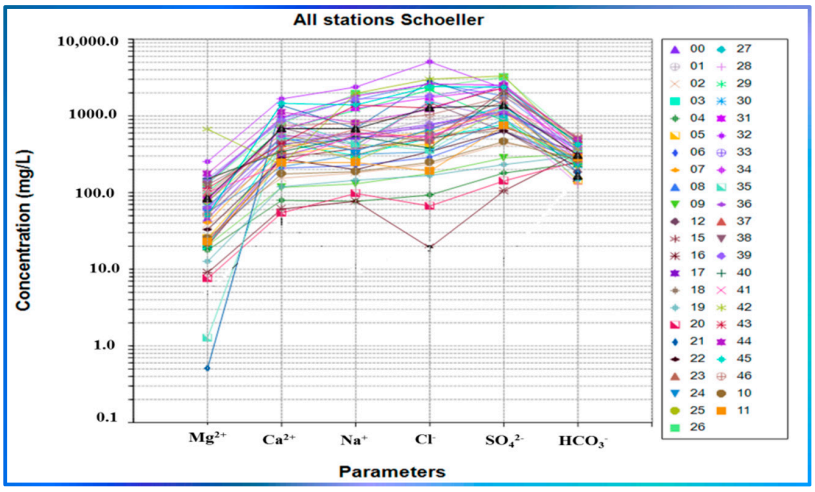

Figure 9. Scholler plot showing the relative major ions distribution throughout the study area.

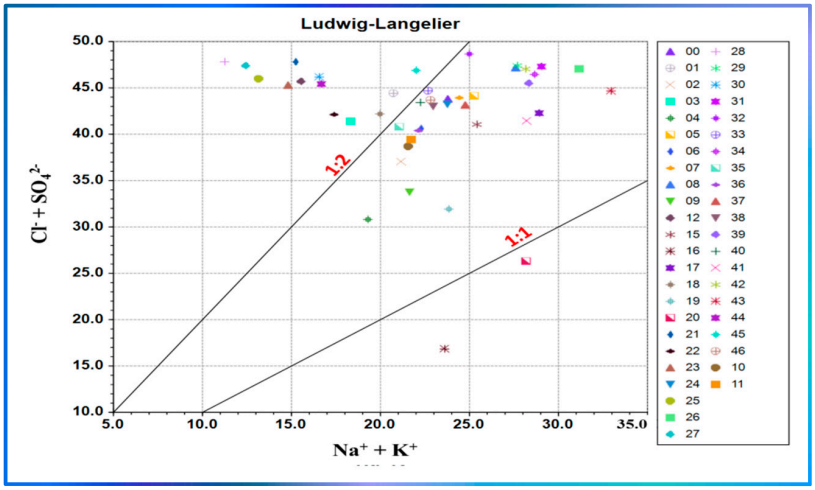

Figure 10. Ludwig–Langelier plot of the patterns and correlations between the major cations and anions throughout the study area.

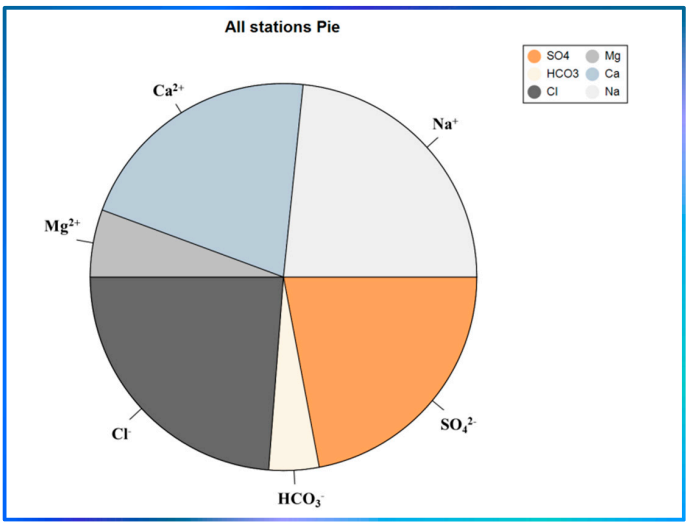

Figure 11. Pie plot comparing the aggregated relative proportions of the major ionic constituents throughout the study area.

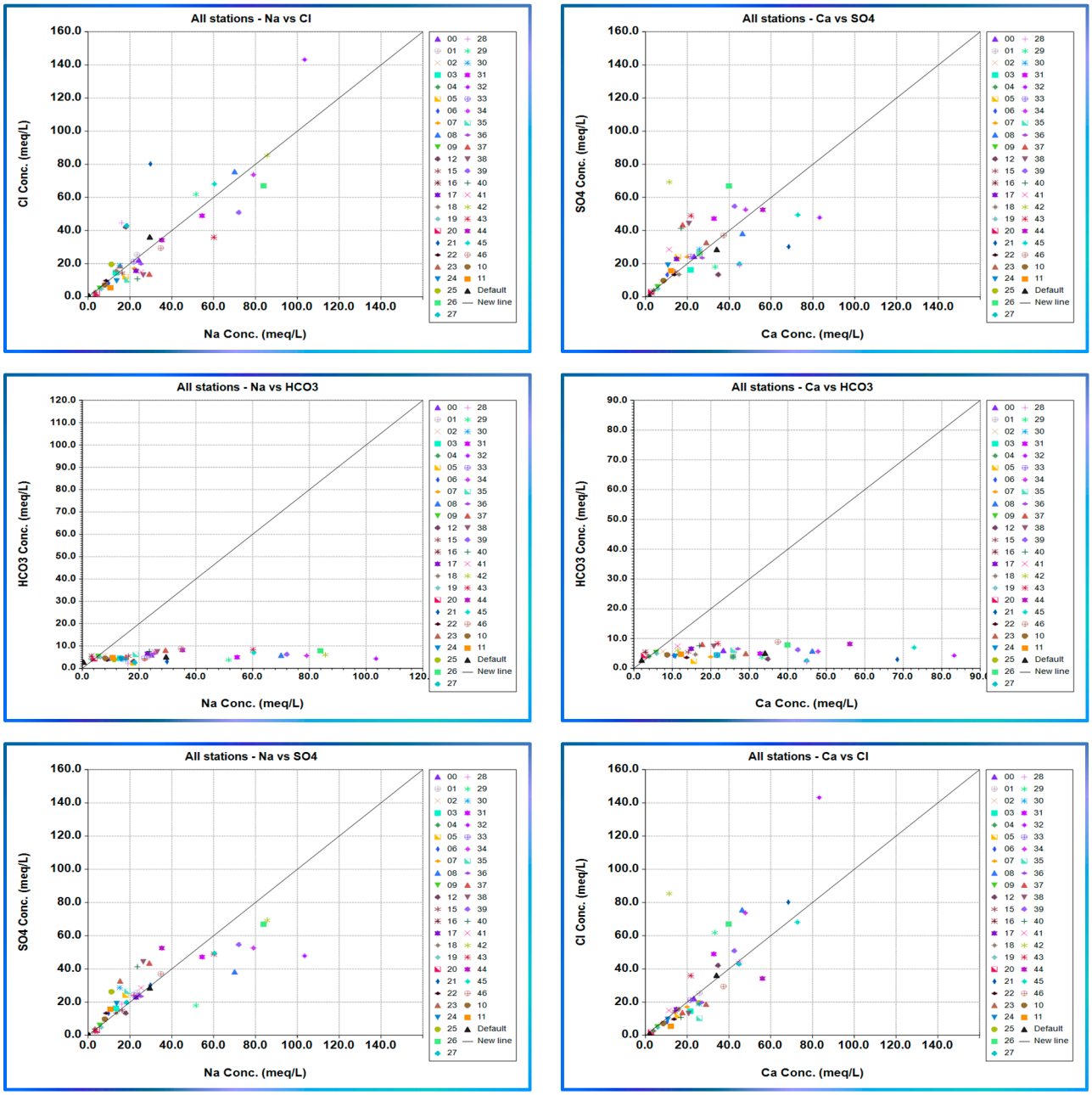

Figure 12. Ionic ratios plots of different combinations among the major constituents throughout the study area.

3.4. Major Ionic Species

The Durov diagram shows comparable distributions to Piper's plot with extra TDS and pH representation, Figure 13. Figure 13 shows that samples with high salinity levels have low pH values and higher Na^+ and Cl^- contents than Ca^{2+} and $SO_4{}^{2-}$. The distribution of major constituents in the lateral triangles is similar to the EC level, especially for cations all over the partitions of the study area. These themes suggest that a process other than a water–rock interaction might be in place due to the modification in water composition, which might be hard to be established through rock weathering alone. Actually, it is not easy to have different sources, e.g., halite, gypsum, and dolomite, which could yield equivalent proportions of the major constituents and approximately constant $HCO_3{}^-$ levels. Evaporation, evaporation-driven precipitation, mixing, ion exchange, and reverse ion exchange might be the probable processes controlling and modifying the water

geochemistry in the study area. The next section's subject is figuring out and capturing the most prominent GW chemistry processes.

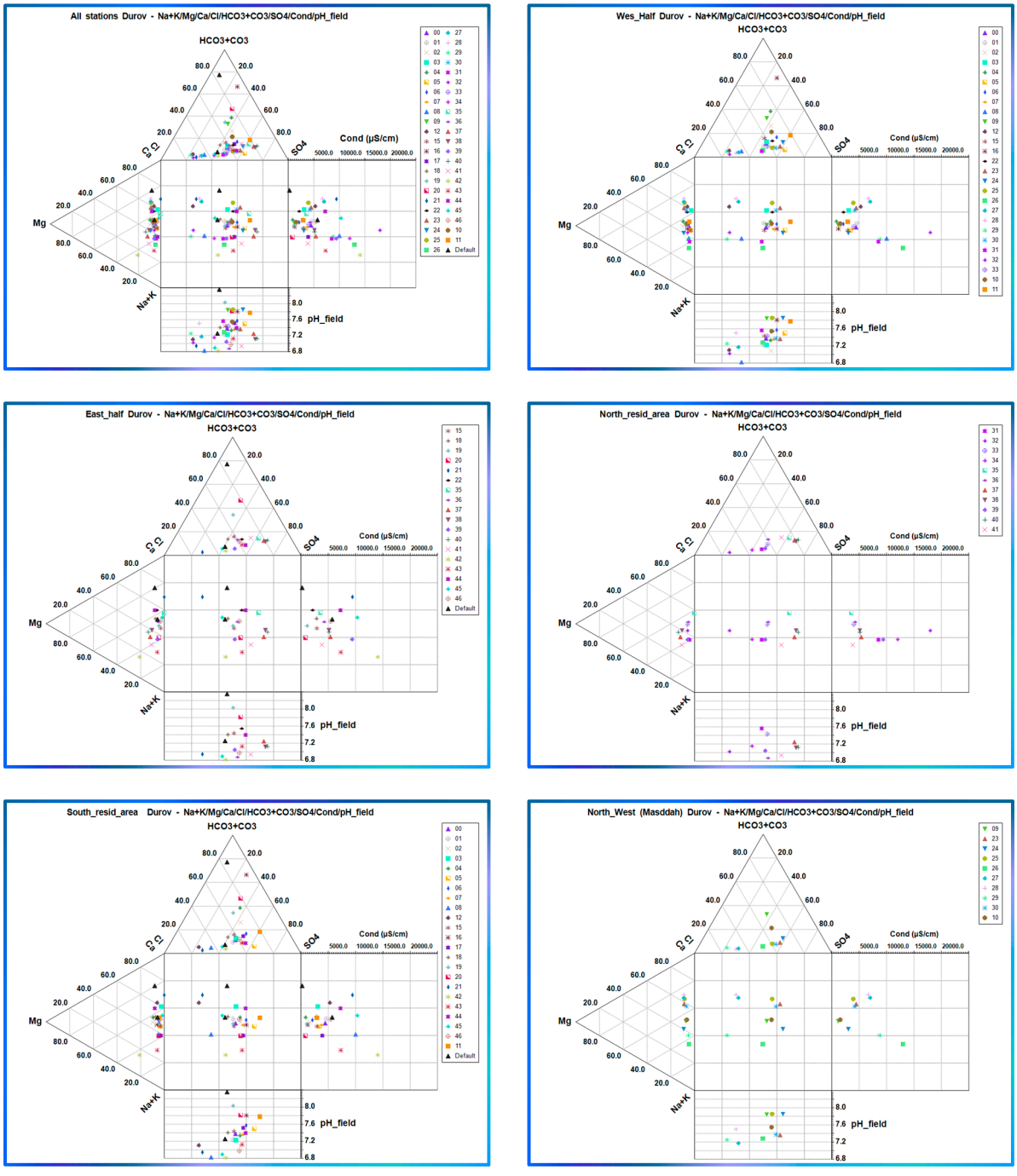

Figure 13. *Cont.*

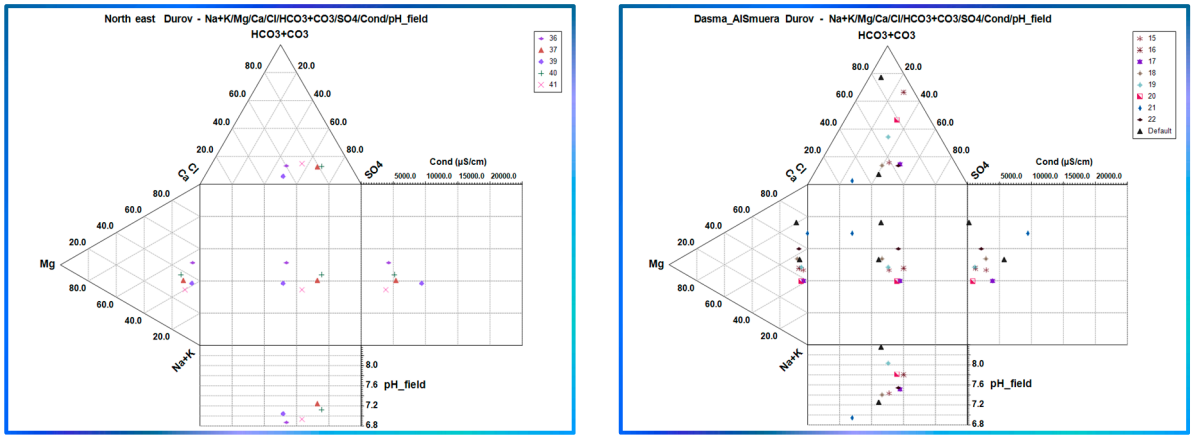

Figure 13. Durov plot represents GW's composition distribution all over the entire study area and the sliced partitions.

3.5. Processes Controlling GW Hydrogeochemistry

The evolution of GW's hydrogeochemistry depends on hosting rock types, flow paths, anthropogenic activities, mixing from different sources, and initial water composition. Evaporation, evaporation-driven precipitation, mixing, ion exchange, and reverse ion exchange might be the probable processes controlling and modifying the water hydrogeochemistry in the study area. Identifying the process/es in place is tried via the Gibbs diagram [62], ion exchange diagram, and other deemed cooperative relationships. Based on the hydrogeochemical data, the Gibbs plot has been widely recognized as a powerful tool to discriminate three distinct processes affecting the GW's chemical composition evolution. The philosophy behind the plot construction is that every process, namely, precipitation, rock–water interaction, and evaporation crystallization dominance, has its fingerprint on one or more of the water characteristics that trace such change or evolution. Gibbs diagram is constructed by plotting the ratio ($Na^+/(Na^+ + Ca^{2+})$) and ($Cl^-/(Cl^- + HCO_3^-)$) on the abscissas against TDS on the ordinate to evaluate the functional variabilities of the ratios of the aforementioned dissolved chemical species demarcating three significant clusters, namely, precipitation dominance, rock dominance, and evaporation dominance. Figure 14 shows that almost all samples fall under the evaporation crystallization dominance zone, except one sample falls away from this zone in the rocks weathering zone in the cation fringe, while two samples fall under the weathering (rock dominance) zone in the anions fringe. So, the Gibbs diagram concludes the impact of the evaporation process. This finding seems logical due to very limited precipitation rates (hyper aridity) and very hot daylight temperatures, implying very high evaporation rates, which exacerbate the ionic loads in the infiltrating irrigation return flow water combined with the re-solubilization of the previously crystallized salts on the soil surface (i.e., the establishment of the vicious salinization cycle). The positive values of saturation indices (SIs, declared later on) corroborate this theme. The Gibbs and Chadah diagrams concluded that hydrochemical GW dominant types in a wide range could be inferred from the Gibbs diagram, while the specific dominant types in specific components would be declared geochemically in the Chadah diagram. Hence, combining the two diagrams would be useful in demarcating the general types and evolutions affecting the GW from the hydrochemistry data.

To further signify the effects of evaporation, the plot of Na/Cl against EC, Figure 15, was constructed and showed that about half of the samples lie around the Na/Cl ratio of one at different levels of EC. However, some other samples exhibited extremely far away Na/Cl ratios ranging from 0.36 to 6.32, demarcating the contributions from distinct sources or processes (i.e., silicate weathering, especially for low EC levels, ion exchange, and reverse ion exchange). This behavior suggests the interplaying of many different processes, which increases the system's complexity. The prominent enrichment of Na^+ ion concentration over Cl^- might be from leaching secondary alkaline/saline soil salts,

irrigation return flow, and partly by silicate weathering [63]. The relationship between ($Na^+ + K^+$) versus T_z^+ yields a trending line with a slope of 0.29 and R^2 0.78, indicating no contribution from secondary sources leaching into the water. In the $Ca^{2+} + Mg^{2+}/HCO_3^-$ equivalent ratio, most samples fall higher than one, indicating that bicarbonate dissolution dominance is not prominent. The spatial distributions of the ratios of $(Na^+ + K^+)/T_z^+$, $(Ca^{2+} + Mg^{2+})/HCO_3^-$, Ca^{2+}/Na^{2+}, Na^+/Cl^-, and EC are portrayed in Figure 16.

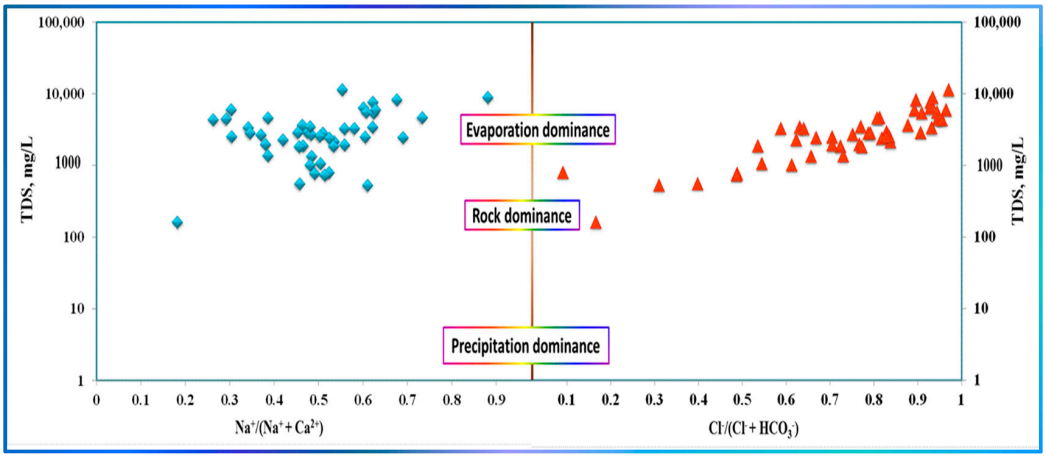

Figure 14. Gibbs plot demarcates the dominance zones of the different water chemistry evolution processes.

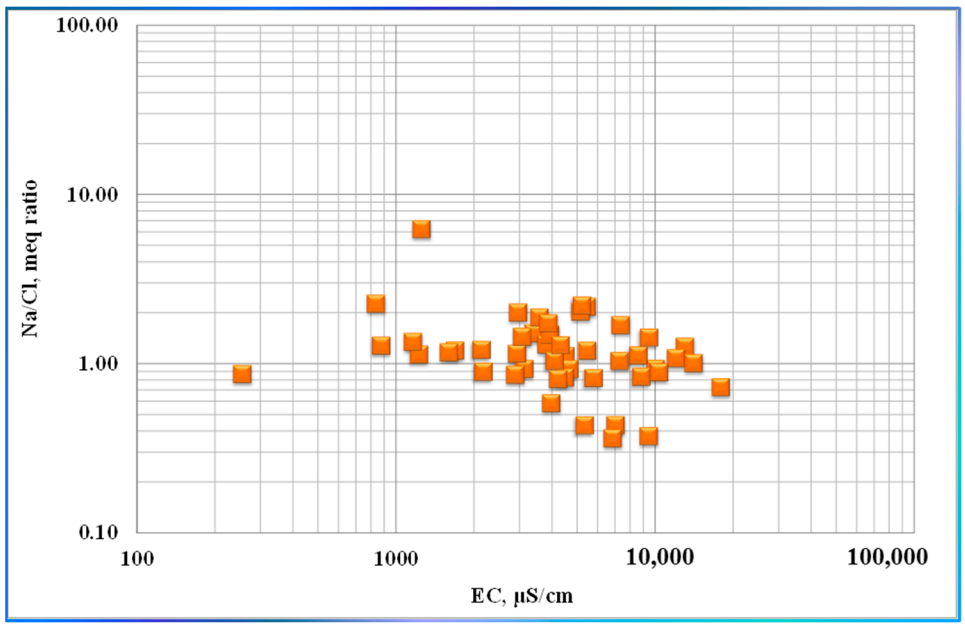

Figure 15. Relationship between Na^+/Cl^- ratio and EC in the study area.

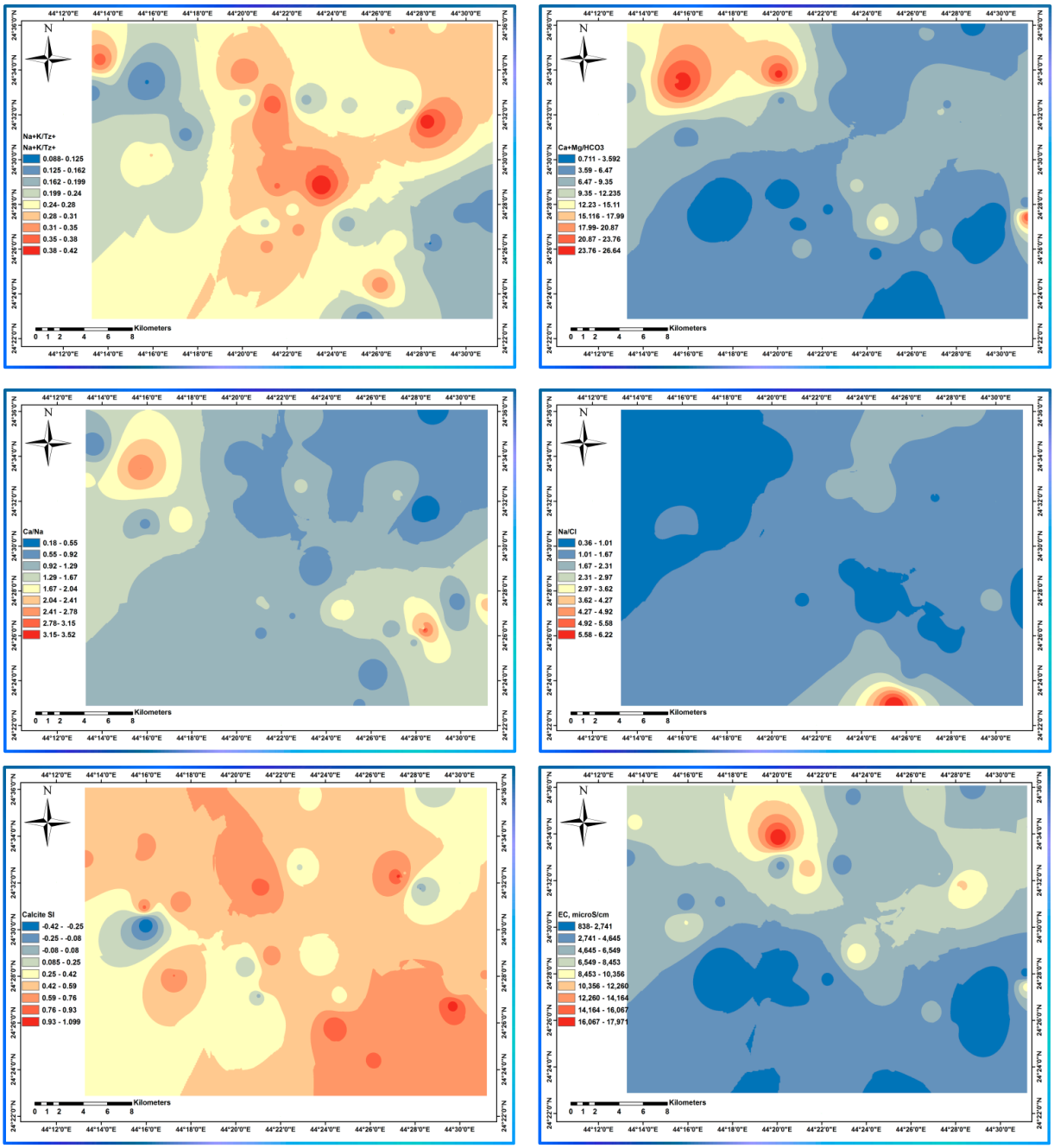

Figure 16. Spatial distributions of $(Na^+ + K^+)/T_z^+$, $(Ca^{2+} + Mg^{2+})/HCO_3^-$, Ca^{2+}/Na^{2+}, Na^+/Cl^-, calcite SI, and EC, respectively.

The distribution of $(Na^+ + K^+)/T_z^+$ spatially varies reversely with $(Ca^{2+}+Mg^{2+})/HCO_3^-$, which may be attributed to the smaller contribution of Ca^{2+} and Mg^{2+} to total cations at higher bicarbonate levels, implying the possible precipitation of calcium and magnesium, and, hence, the enhanced contribution of sodium and potassium to the total cations. The portions exhibiting a higher $(Ca^{2+} + Mg^{2+})/HCO_3^-$ ratio, the northwestern portion, show low to moderate $(Na^+ + K^+)$ contributions to the total cations. Moreover, calcite SI exhibited a trendy inverse distribution with $(Na^+ + K^+)/T_z^+$, $(Ca^{2+} + Mg^{2+})/HCO_3^-$, and Ca^{2+}/Na^{2+}. On the contrary, the interpolated spatial distribution of Na^+/Cl^- and $(Na^+ + K^+)/T_z^+$ is in direct accordance, implying that Na^+ and Cl^- might originate from a common source. Finally, all those distributions seem independent of the total salinity, EC. The contribution regression

of the individual cations and anions with the EC (Figure 17) confirmed sodium contribution's linearity with a slope of 0.13 and R^2 0.88.

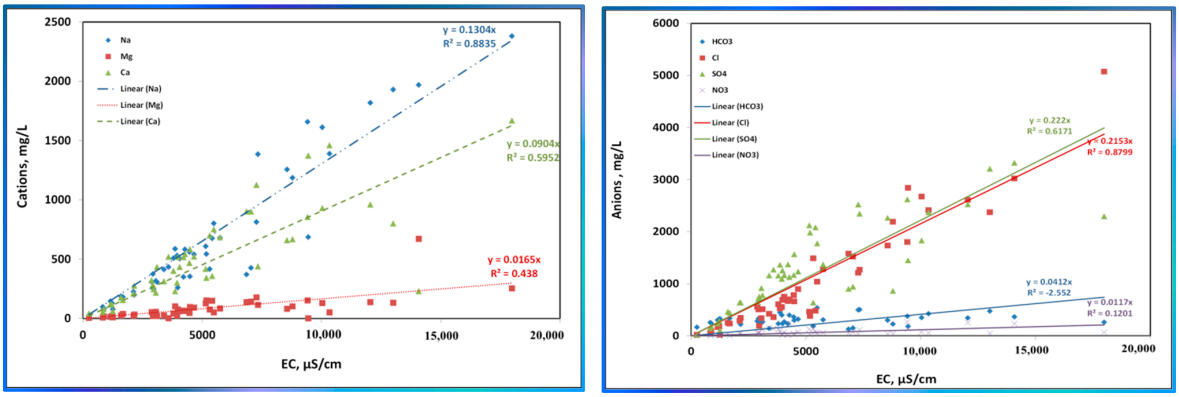

Figure 17. Individual major ions contribution to the total EC of the GW samples throughout the study area.

On the contrary, calcium and magnesium showed lower regression coefficients of 0.59 and 0.438, respectively. The regression coefficients of chloride, sulfate, bicarbonate, and nitrate are 0.88, 0.617, −2.5, and 0.12, respectively. Higher regression coefficients are observed for the conservative and quasi-conservative ions. This theme may suggest that the hydrogeochemical composition of the GW system may be largely impacted by concentrating and modifying processes along with the weathering ones.

Investigating the contribution and effects of the weathering reactions in the study area has been attempted to infer the probable sources affecting the processes of the major ions in GW's chemistry. Figure 18A,B portray the effects of weathering and geochemical processes, respectively. Most samples are affected by silicate weathering and Gypsum dissolution, with only a few samples lying in the carbonate/dolomite and evaporate dissolution fringes. Moreover, about one-third of the samples are impacted by calcium salt precipitation and/or reverse ion exchange. The geochemical modeling results corroborate calcium salt precipitation, as the saturation indices (detailed in the next section) of aragonite, calcite, dolomite (ordered and disordered), gypsum, and anhydrate are mostly positive.

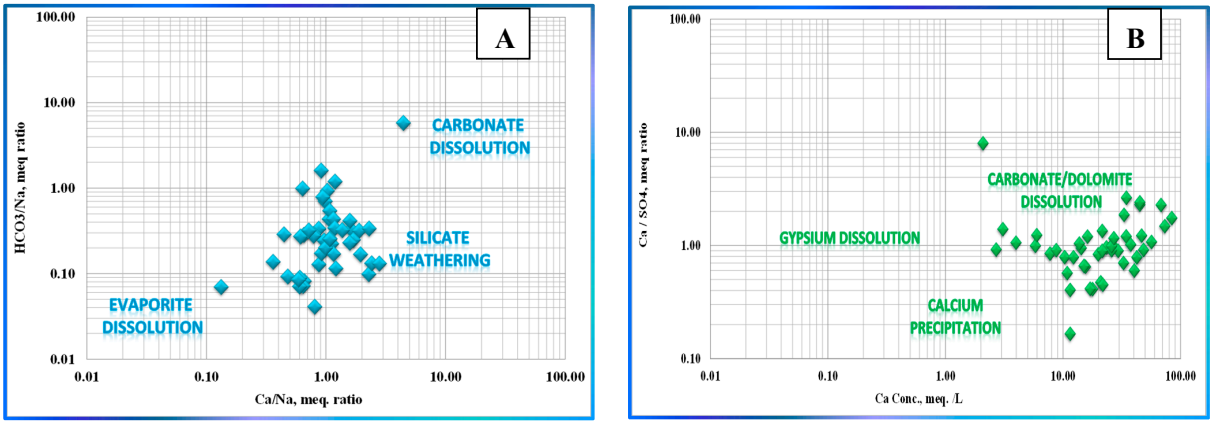

Figure 18. Clustering of the effects of weathering (**A**) and geochemical processes (**B**).

3.6. Ion Exchange Process

The ion exchange process (IX) does not change the dissolved species' total load but rather alters the concentration of individual water chemistry parameters, mainly Ca^{2+} and Na^{+}. Two chloro-alkaline indices (CAI-1 and CAI-2) were inferred by Schoeller [64] to demarcate the IX processes between the GW and its host environment; as such, the positive

values of these indices mark the direct replacement of Clay-Na^+ by the higher affinity Ca^{2+} ions, whereas the negative values denote the reverse [14,48,64]. The chloro-alkaline indices are calculated using the following formulas:

$$CAI\text{-}1 = [Cl^- - (Na^+ + K^+)/Cl^-]$$

and

$$CAI\text{-}2 = [Cl^- - (Na^+ + K^+)]/(SO_4{}^{2-} + HCO_3{}^- + CO_3{}^{2-} + NO_3{}^-).$$

All concentrations are in meq/L. The inverse distance weighted (IDW) interpolated spatial distribution map of the calculated indices along with that of Na^+ and Ca^{2+} ions concentrations are in Figure 19. The spatial distribution of the indices indicated no clear linkage between the distribution of sodium and the indices contrary to that of calcium concentration. A quasi-coincidence between calcium distribution and CAI-1 is apparent. Furthermore, the areas showing negative CAI-1 and CAI-2 values spread over 20–30% of the area, indicating the prevalence of reverse ion exchange in such areas that exhibit the highest localities of sodium ion concentration distribution. The relationship in Figure 20 corroborates those findings. Figure 20 concludes that the direct and reveres ion-exchange occurrence is evident with a trending line slope of −1.06 and R^2 0.845, with ≈28% of the samples falling under the reverse ion exchange part and ≈50% in the direct-ion exchange part. The spatial distributions and the relationship in Figure 20 complement each other with close agreements on their quantitative conclusions regarding the shared percentages of the direct and reverse ion exchange.

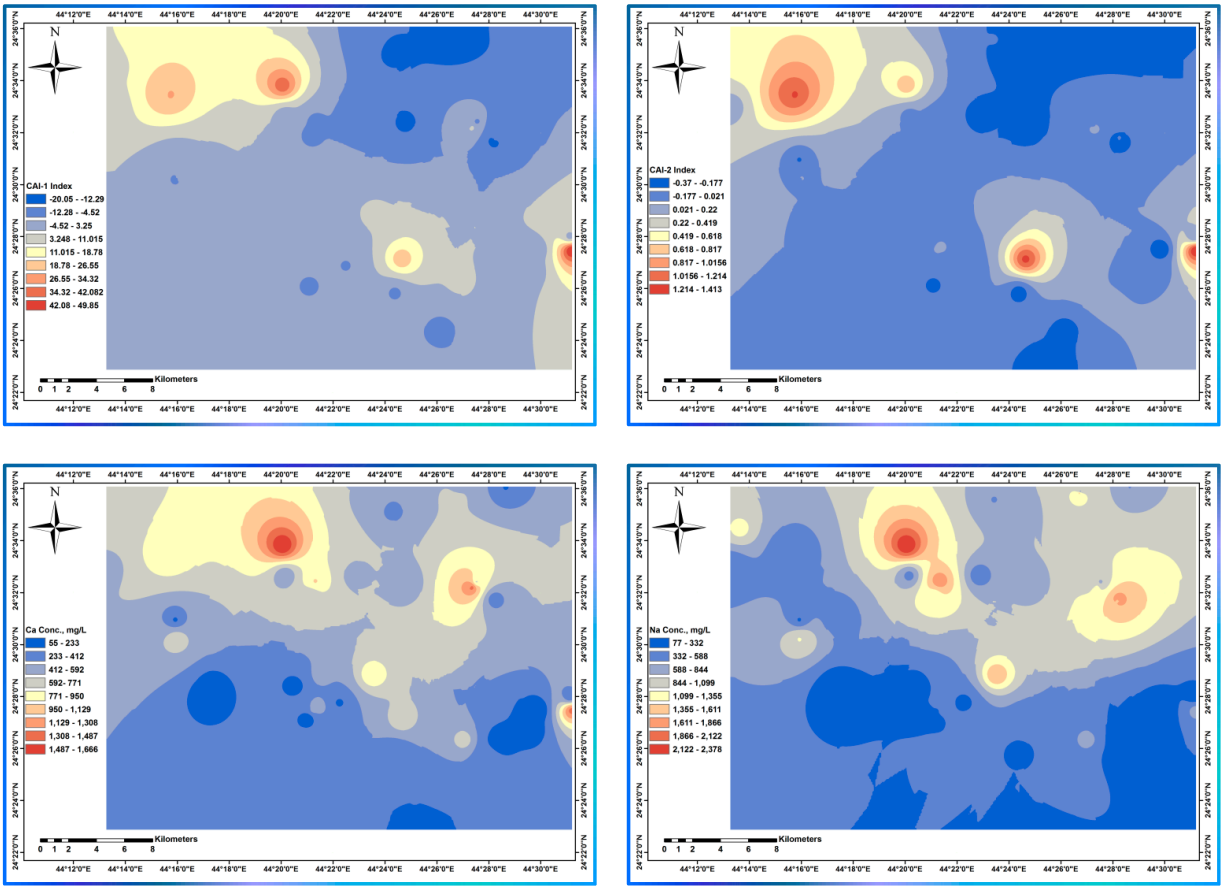

Figure 19. Inverse distance weighted interpolated spatial distribution of the CAI-1, CAI-2, Ca^{2+} concentration, and Na^+ concentration. CAI-1 = $[Cl^- - (Na^+ + K^+)/Cl^-]$; and CAI-2 = $[Cl^- - (Na^+ + K^+)]/(SO_4{}^{2-} + HCO_3{}^- + CO_3{}^{2-} + NO_3{}^-)$; all concentrations are in meq/L.

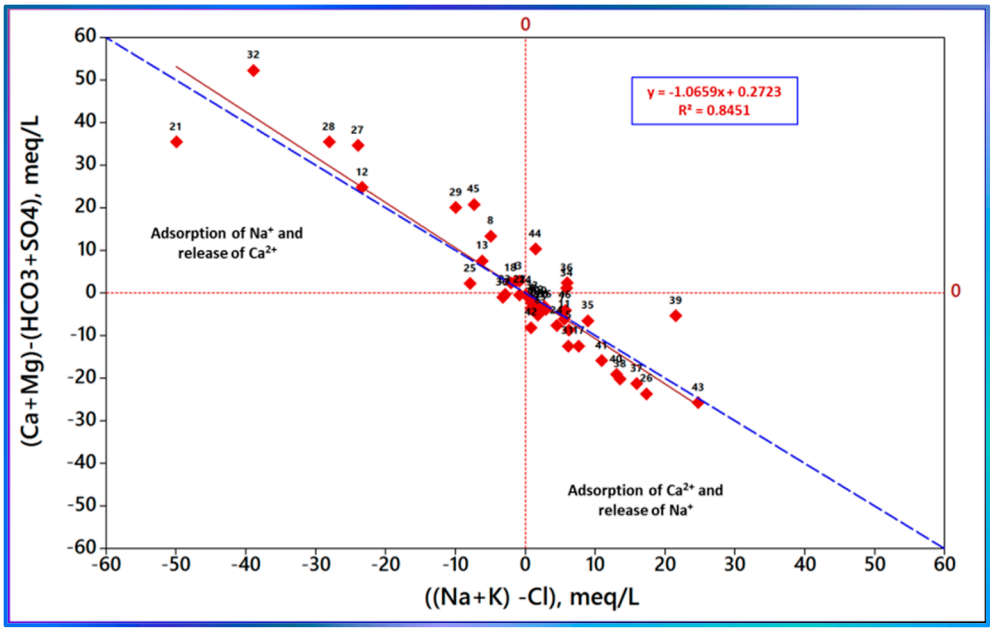

Figure 20. Direct and reverse ion exchange occurrence and the shared percentages throughout the study area.

3.7. Hydrogeochemical Analysis Using Visual MINTEQ

Visual MINTEQ was used to calculate the saturation index (SI) of various minerals, namely, anhydrite, aragonite, artinite, brucite, gypsum, halite, calcite, dolomite (ordered and disordered), epsomite, huntite, lime, magnesite, and vaterite to determine whether the GW system is oversaturated, undersaturated, or at equilibrium, concerning the studied minerals. The values of the SIs determine the tendency of the system to dissolve or precipitate such minerals. The descriptive statistics summary of the Visual MINTEQ calculated SIs are supplied in Table 2 and Figure 21 in box plot form. The geochemical modeling program Visual MINTEQ computes the SIs, assuming that the "n" solid phase was originally present in the medium based on the GW chemical composition, pH, and temperature. The computed indices, SIs, namely, SIs in the range of −0.5 to +0.5, are considered to pose no potential risk of dissolution or precipitation, and SIs less than −0.5 presume that the solution is undersaturated, showing the tendency of the solution to dissolve more of that mineral whenever it is present in the aquifer, and the reverse, oversaturation with the tendency of precipitation when SI > +0.5. An SI of approximately zero indicates that equilibrium or saturation conditions between the solution and the mineral, with no reaction, are expected [54].

The data show that the SIs are not normally distributed with as high skewness and Kurtosis values as those from the original data, except for that of halite, which exhibits the lowest skewness and Kurtosis values. This trend may suggest significant processes that impact major individual constituents that may undergo input/output (solubilization/precipitation) effects. Large Kurtosis values indicate the presence of some extreme localities that lead to large differences between the median and mean values. Anhydrite, artinite, brucite, halite, epsomite, huntite, lime, gypsum, and magnesite minerals exhibited negative SIs, indicating that the GW system is undersaturated concerning those minerals. The undersaturation status exhibited for areas with the most negative halite, anhydrate, and gypsum SI values would potentially increase the Cl^-, SO_4^{2-}, and salinity in GW with water flow due to the large dissolution affinity of such minerals. The other aragonite, calcite, dolomite (ordered and disordered), and vaterite minerals showed positive SIs values. The points exhibiting the most positive SI values would have a larger potential for precipitation of the respective minerals, such as aragonite, calcite, and ordered dolomite. Significant SO_4^{2-} and Ca^{2+} that might precipitate to the soil and $CaCO_3$ saturation were observed in

the semi-arid and arid areas [58], leading to concentration-driven evaporation due to the aridity and higher weather temperatures. Such processes, coupled with the ion exchange, would greatly impact and modify the chemical composition of the GW and affect the aquifer and soil properties such as permeability. The results of the SIs are consistent with the GW's sodium, chloride, calcium, and sulfate levels.

Table 2. Descriptive statistics of the SIs of the main anticipated minerals.

Variable	Mean	SE Mean	StDev	Min.	Q1	Median	Q3	Max.	Range	IQR	Skewness	Kurtosis
Anhydrite	−0.7087	0.0799	0.5480	−2.8470	−0.8260	−0.5540	−0.3950	−0.0400	2.8070	0.4310	−1.80	4.20
Aragonite	0.3617	0.0584	0.4004	−1.7050	0.2820	0.4230	0.5540	0.9630	2.6680	0.2720	−3.22	15.24
Artinite	−6.630	0.188	1.288	−11.873	−7.110	−6.417	−6.068	−4.785	7.088	1.042	−2.43	8.04
Brucite	−5.477	0.116	0.793	−8.129	−5.760	−5.385	−5.057	−4.228	3.901	0.703	−1.44	3.69
Calcite	0.5039	0.0583	0.4000	−1.5600	0.4210	0.5700	0.6950	1.1070	2.6670	0.2740	−3.22	15.23
Dolomite disordered	−0.045	0.128	0.877	−3.680	−0.312	0.181	0.351	1.235	4.915	0.663	−2.44	7.44
Dolomite ordered	0.495	0.128	0.877	−3.141	0.229	0.731	0.885	1.785	4.926	0.656	−2.45	7.50
Epsomite	−3.642	0.103	0.704	−5.770	−3.915	−3.500	−3.153	−2.290	3.480	0.762	−1.25	2.09
Gypsum	−0.4718	0.0797	0.5466	−2.5980	−0.5930	−0.3200	−0.1660	0.1980	2.7960	0.4270	−1.80	4.17
Halite	−5.234	0.130	0.891	−8.216	−5.510	−5.183	−4.725	−3.697	4.519	0.785	−1.04	2.02
Huntite	−3.853	0.300	2.057	−11.662	−4.470	−3.308	−2.850	−1.200	10.462	1.620	−2.51	7.01
Lime	−20.299	0.0953	0.653	−21.780	−20.760	−20.260	−19.871	−19.037	2.743	0.889	−0.16	−0.43
Magnesite	−1.109	0.147	1.005	−3.912	−1.322	−1.080	−0.890	4.237	8.149	0.432	2.62	18.75
Vaterite	−0.0390	0.0588	0.4033	−2.1250	−0.1240	0.0010	0.1520	0.5410	2.6660	0.2760	−3.23	15.43

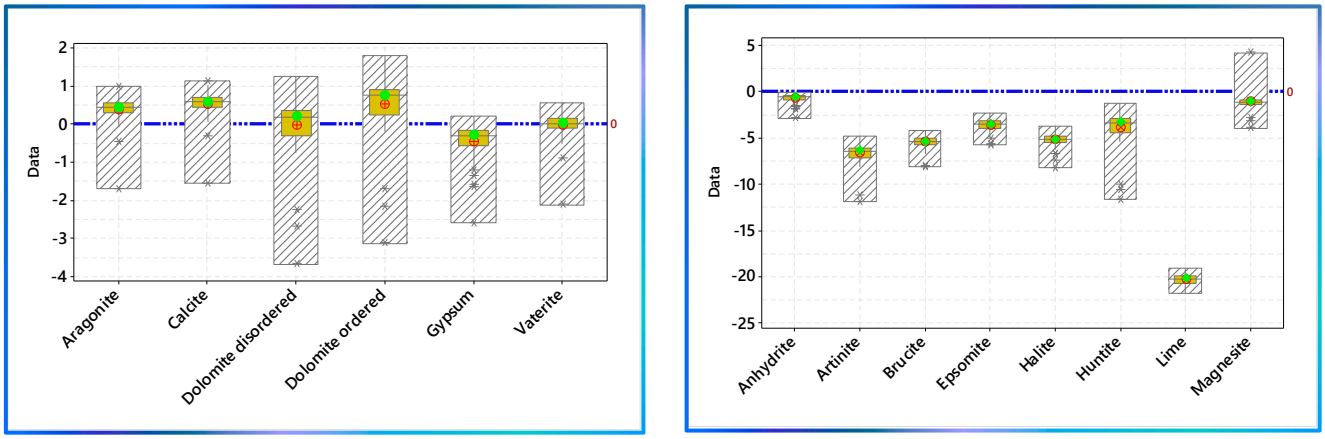

Figure 21. Box plot of the SIs of considered minerals distribution.

3.8. Correlation Statistical Analysis

The spearman rho correlation analysis was computed using Minitab@18, Table 3, to check the correlation between physiochemical water parameters such as temperature, pH, EC, major cations, and major anions. The scaling terms are considered as the following: $r < 0.5$ weak correlations, $0.5 > r < 0.7$ moderate correlation, and strong correlation refer to $r > 0.7$, provided that the p-values are < 0.05. The positive correlation values (colored red in Table 3) refer to the direct relationship between the tested parameters and vice versa (inverse relationship colored green in Table 3). As logically expected, the correlation analysis showed that Na+, Ca^{2+}, Mg^{2+}, Cl^{-}, and $SO_4{}^{2-}$ concentrations strongly correlate with EC; they may be considered strong predictors for EC GW. Moreover, K^{+} and $NO_3{}^{-}$ exhibited a moderate correlation with EC, expected for K^{+}, since the rock-containing abundance is usually limited and dominated by Na^{+}-containing ones. pH showed a moderate negative correlation with most of the tested physicochemical parameters.

Table 3. Spearman Rho correlation matrix.

Parameters	Na^+	K^+	Ca^{2+}	Mg^{2+}	NH_4^+	HCO_3^-	Cl^-	SO_4^{2-}	NO_3^-	EC, µS/cm	Temp., °C	pH	Anderson–Darling Normality Test	
													p-Value	Inference
K^+	0.552												<0.005	Fail
p-Value	0.000													
Ca^{2+}	0.740	0.671											<0.005	Fail
	0.000	0.000												
Mg^{2+}	0.695	0.506	0.558										<0.005	Fail
	0.000	0.000	0.000											
NH_4^+	−0.510	−0.142	−0.341	−0.511									<0.005	Fail
	0.000	0.342	0.019	0.000										
HCO_3^-	0.493	−0.117	0.110	0.308	−0.369								0.474	Pass
	0.000	0.432	0.464	0.035	0.011									
Cl^-	0.856	0.756	0.873	0.653	−0.354	0.120							<0.005	Fail
	0.000	0.000	0.000	0.000	0.015	0.423								
SO_4^{2-}	0.892	0.498	0.682	0.715	−0.598	0.536	0.731						0.072	Pass
	0.000	0.000	0.000	0.000	0.000	0.000	0.000							
NO_3^-	0.599	0.465	0.472	0.328	−0.136	0.152	0.528	0.489					<0.005	Fail
	0.000	0.001	0.001	0.024	0.362	0.307	0.000	0.000						
EC, µS/cm	0.928	0.676	0.856	0.760	−0.482	0.294	0.938	0.859	0.517				<0.005	Fail
	0.000	0.000	0.000	0.000	0.001	0.045	0.000	0.000	0.000					
Temp., °C	0.042	0.137	0.131	0.095	−0.165	−0.176	0.122	−0.005	−0.050	0.136			0.011	Fail
	0.780	0.357	0.380	0.523	0.268	0.237	0.416	0.975	0.739	0.363				
pH	−0.670	−0.373	−0.543	−0.415	0.331	−0.425	−0.574	−0.578	−0.654	−0.622	0.113		0.321	Pass
	0.000	0.010	0.000	0.004	0.023	0.003	0.000	0.000	0.000	0.000	0.448			
WD *, m bgl **	0.108	−0.073	0.135	0.141	−0.103	0.349	−0.033	0.136	0.007	0.091	0.15	−0.158		
	0.472	0.627	0.367	0.345	0.49	0.016	0.827	0.361	0.965	0.542	0.912	0.290		

The numbers in red indicate a worsening effect (positive correlation); the green one indicates an alleviation effect (negative correlation); the blue colored numbers indicate no correlation. * well depth, ** meter below ground level.

Nevertheless, it is worth noting NO_3^-, where we find that it was not localized due to point sources but was widespread in most of the study area. HCO_3^- showed a weak correlation to EC, which was not expected since the concentration of HCO_3^- ranges from 128.9 to 536 with a mean of 314.9 and stdev of ±102.8 mg/L (i.e., there is a large share of HCO_3^- to the total ions load of the samples). A probable explanation is that HCO_3^- was affected by, and underwent, different hindering processes, following the same trend as EC; i.e., it did not ramp linearly by evaporation as it may have followed up-and-down variation paths as it is largely dependent on pH levels. This explanation may be corroborated by the findings of the Anderson–Darling normality test, which showed that HCO_3^- passes (i.e., follow a normal distribution) with a *p*-value of 0.474, contrary to that of EC, which failed at a *p*-value < 0.005. The concentrations of the constituents that underwent continuous unidirectional (input or output) is expected to ramp (or decline) to one-tail, which means it does not follow the normal distribution. A final inference may be that evaporation concentration played a major role in the chemistry of the GW system under consideration, supporting the findings of the Gibbs diagram, Figure 14, with HCO_3^- continuously removed when reaching a certain limit through precipitation as calcite, aragonite, and dolomite, with the positive SIs for carbonate-containing minerals further corroborating the explanation of this notable trend. The highest correlation coefficients >0.9 were noted for the conservative Cl^- and quasi-conservative Na^+ ions, further supporting that evaporation significantly impacts the system. The r of Na^+ and Ca^{2+} is 0.74 (i.e., lower than that of Na^+ and Cl^- with EC). Although there is no straightforward correlation coefficient between them, this supports that calcium is not ramping at the same rate as that of Cl^- and Na^+ due to evaporation, denoting its probable removal path through precipitation as indicated by the positive SIs of the calcium-containing minerals. Moreover, direct ion exchange may share such findings that the reverse ion exchange may compensate partially for the effect of direct ion exchange. Overall, direct and reverse ion exchange processes have a mild effect compared to that of evaporation since there is no common mineral resource for calcium and sodium to attribute their concurrent ramping to that of rock dissolution. Well depth showed no correlation except a mild worsening with HCO_3^-. However, it is believed that well depth may have an apparent correlation with the water chemistry variables, but, unfortunately, they are hidden due to averaging the correlation matrix over the whole study area, which experienced local

variabilities. So, many other prominent correlations may appear if the correlation matrix is prepared over sliced portions. Such slicing on the correlation matrix was not performed for the current work due to time constraints, but it may be formulated with more details in upcoming work.

Such slicing on the correlation matrix was not performed for the current work to avoid more lengthy, but it may be formulated with more details in upcoming work.

4. Conclusions

This study integrates GIS, statistical, and graphical approaches to evaluate the hydrogeochemical status and understand the implications of evaporation, rock–water interactions, and the interplaying factors in the AdDawadmi region, Saudi Arabia. The study complemented, integrated, corroborated, and/or declined the findings of each approach alone and portrayed an overall picture of the major players that control the geochemical evolution in the study area. The concluding remarks, which are made with a general scope sense rather than with specific local-relevant numbers, are summarized as follows:

a. Many co-occurring processes control the GW system's evolution in the region: anthropogenic-driven evaporation, ion exchange (direct and reverse), precipitation of calcium salts, dissolution of soil salts, and rock weathering.
b. The establishment of the vicious salinization cycle due to hyper-aridity, intensive agricultural activities, and higher daylight temperatures. This cycle poses immense deteriorating stresses on the quality of the GW reserve in the region.
c. Partitioning the study area into small portions on a spatial basis aided in mining useful information, allowing demarcating variations among localities in the case of relationships lacking spatial distribution ability such as Piper, radial, and Durov plots.
d. The Hydrogeochemical modeling inferred the oversaturation of many minerals due to higher levels of EC and pH. The computed SIs are not normally distributed with as high skewness and Kurtosis values as those from the original data except for those of halite, which exhibit the lowest skewness and Kurtosis values, suggesting the existence of significant processes that impact the major individual constituents that may undergo input/output (solubilization/precipitation) effects.
e. The largest regression and correlation coefficients are observed for the conservative and quasi-conservative ions, further supporting that evaporation significantly impacts the system.
f. Localities exhibiting peaks of ECs, NO_3^-, SO_4^{2-}, Cl^-, Na^+, and Ca^{2+} are identified, demarcating the effects of localized point source activities and evaporation-driven concentrating processes rather than those of lithology, catchment, or basin-wise ones.
g. Integrating different approaches constrained the findings and interpretations, providing multiple lines of evidence that usefully supported or declined those that might be masked.
h. Human activities, mainly agriculture, greatly impact the region's GW system. Hence, remediation plans and protection policies to be in place are highly recommended to prevent overexploitation of the reserve and, simultaneously, remediate and brook the established vicious salinization cycle.
i. Implementing and even enforcing recent irrigation systems' adoption by the region's peoples could help relieve the continuous ramping problem.

Author Contributions: H.E.G.: conceptualization, methodology, software, validation, formal analysis investigation, resources, data curation, writing—original draft preparation, supervision, project administration, and funding acquisition. A.A.A.: methodology, validation, resources, data curation, and writing—review and editing. M.C.: methodology, validation, formal analysis, and writing—review and editing. F.A.G.: conceptualization, methodology, software, investigation, data curation, writing—original draft preparation, and writing—review and editing. All authors have read and agreed to the published version of the manuscript.

Funding: The authors extend their appreciation to the Deputyship for Research and Innovation, Ministry of Education in Saudi Arabia, for funding this research work through project number (IFP-2021-062).

Institutional Review Board Statement: Not applicable.

Informed Consent Statement: Not applicable.

Data Availability Statement: Not applicable.

Conflicts of Interest: The authors declare no conflict of interest. The funders had no role in the design of the study; in the collection, analyses, or interpretation of data; in the writing of the manuscript, or in the decision to publish the results.

References

1. Kajenthira, A.; Siddiqi, A.; Anadon, L.D. A new case for promoting wastewater reuse in Saudi Arabia: Bringing energy into the water equation. *J. Environ. Manag.* **2012**, *102*, 184–192. [CrossRef]
2. Drewes, J.; Garduño, C.; Amy, G. Water reuse in the kingdom of Saudi Arabia—Status, prospects, and research needs. *Water Sci. Technol. Water Supply* **2012**, *12*, 926–936. [CrossRef]
3. FAO. *Irrigation in the Middle East Region in Figures: AQUASTAT Survey 2008*; FAO Water Reports; FAO: Roma, Italy, 2008.
4. Chowdhury, S.; Al-zahrani, M. Implications of Climate Change on Water Resources in Saudi Arabia. *Arab. J. Sci. Eng.* **2013**, *38*, 1959–1971. [CrossRef]
5. Chowdhury, S.; Al-zahrani, M. Characterizing water resources and trends of sector-wise water consumptions in Saudi Arabia. *J. King Saud Univ. Eng. Sci.* **2013**, *27*, 68–82. [CrossRef]
6. Chowdhury, S.; Al-zahrani, M. Water Resources And Water Consumption Pattern In Saudi Arabia. In Proceedings of the 10th Gulf Water Conference, Doha, Qatar, 22–24 April 2012; pp. 67–81.
7. Haider, H.; Ghumman, A.; Al-salamah, I.; Thabit, H. Assessment Framework for Natural Groundwater Contamination in Arid Regions: Development of Indices and Wells Ranking System Using Fuzzy VIKOR Method. *Water* **2020**, *12*, 423. [CrossRef]
8. Wang, J.; Yang, Y. An approach to catchment-scale groundwater nitrate risk assessment from diffuse agricultural sources: A case study in the Upper Bann, Northern Ireland. *Hydrol Process.* **2008**, *4286*, 4274–4286. [CrossRef]
9. Al-Zaidi, A.; Elhag, E.; Al-Otaibi, S.; Baig, M. Negative effects of pesticides on the environment and the farmers awareness in Saudi Arabia: A case study. *J. Anim. Plant Sci.* **2011**, *21*, 605–611.
10. Alhawas, A.A. Towards sustainable water resources for arid land cities: The case of Riyadh. *WIT* **2011**, *145*, 87–98. [CrossRef]
11. Alrasheedi, N.H. An Analysis of Renewable Water Sources in Saudi Arabia. *Am. J. Clim. Chang.* **2014**, *3*, 413–419. [CrossRef]
12. Benaafi, M.; Al-shaibani, A. Hydrochemical and Isotopic Investigation of the Groundwater from Wajid Aquifer in Wadi Al-Dawasir, Southern Saudi Arabia. *Water* **2021**, *13*, 1855. [CrossRef]
13. Zaidi, F.; Mogren, S.; Mukhopadhyay, M.; Ibrahim, E. Evaluation of groundwater chemistry and its impact on drinking and irrigation water quality in the eastern part of the Central Arabian graben and trough system, Saudi Arabia. *J. African Earth Sci.* **2016**, *120*, 208–219. [CrossRef]
14. Kumar, P.; Mahajan, A.; Kumar, A. Groundwater geochemical facie: Implications of rock-water interaction at the Chamba city (HP), northwest Himalaya, India. *Environ. Sci. Pollut. Res.* **2020**, *27*, 9012–9026. [CrossRef]
15. Dehnavi, A.G.; Sarikhani, R.; Nagaraju, D. Hydro geochemical and rock water interaction studies in East of Kurdistan, NW of Iran. *Int. J. Environ. Sci Res.* **2011**, *1*, 16–22.
16. Subramani, T.; Rajmohan, N.; Elango, L. Groundwater geochemistry and identification of hydrogeochemical processes in a hard rock region, Southern India. *Environ. Monit. Assess.* **2010**, *162*, 123–137. [CrossRef]
17. Su, Y.-H.; Feng, Q.; Zhu, G.-F.; Si, J.-H.; Zhang, Y.-W. Identification, and Evolution of Groundwater Chemistry in the Ejin Sub-Basin of the Heihe River, Northwest China. *Pedosphere* **2007**, *17*, 331–342. [CrossRef]
18. Ren, C.; Zhang, Q. Groundwater Chemical Characteristics and Controlling Factors in a Region of Northern China with Intensive Human Activity. *Int. J. Environ. Res. Public Health* **2020**, *17*, 9126. [CrossRef] [PubMed]
19. Biglari, H.; Chavoshani, A.; Javan, N.; Mahvi, A.H. Geochemical study of groundwater conditions with special emphasis on fluoride concentration, Iran, Desalin. *Water Treat.* **2016**, *57*, 22392–22399. [CrossRef]
20. Glynn, P.; Plummer, L. Geochemistry and the understanding of ground-water systems. *Hydrogeol. J.* **2005**, *13*, 263–287. [CrossRef]
21. Herczeg, A.L.; Dogramaci, S.S.; Leaney, F.W.J. Origin of dissolved salts in a large, semi-arid groundwater system: Murray Basin, Australia. *Mar. Freshw. Res.* **2001**, *52*, 41–52. [CrossRef]
22. Nachshon, U.; Weisbrod, N.; Dragila, M.; Grader, A. Combined evaporation and salt precipitation in homogeneous and heterogeneous porous media. *Water Resour. Res.* **2011**, *47*, 1–16. [CrossRef]
23. Abbasnia, A.; Alimohammadi, M.; Mahvi, A.H.; Nabizadeh, R.; Yousefi, M.; Pasalari, H.; Mirzabeigi, M. Assessment of groundwater quality and evaluation of scaling and corrosiveness potential of drinking water samples in villages of Chabahr city, Sistan and Baluchistan province in Iran. *Data Brief* **2018**, *16*, 182–192. [CrossRef]
24. Ijumulana, J.; Ligate, F.; Bhattacharya, P.; Mtalo, F.; Zhang, C. Spatial analysis and GIS mapping of regional hotspots and potential health risk of fluoride concentrations in groundwater of northern Tanzania. *Sci. Total Environ.* **2020**, *735*, 139584. [CrossRef]

25. Fatima, S.; Khan, M.; Siddiqui, F.; Mahmood, N.; Salman, N.; Alamgir, A.; Shaukat, S. Geospatial assessment of water quality using principal components analysis (PCA) and water quality index (WQI) in Basho Valley, Gilgit Baltistan (Northern Areas of Pakistan). *Environ. Monit. Assess.* **2022**, *194*, 151. [CrossRef]
26. Mohamed, A.; Asmoay, A.; Alshehri, F.; Abdelrady, A.; Othman, A. Hydro-Geochemical Applications and Multivariate Analysis to Assess the Water–Rock Interaction in Arid Environments. *Appl. Sci.* **2022**, *12*, 6340. [CrossRef]
27. Ahmed, I.; Nazzal, Y.; Zaidi, F.K.; Al-Arifi, N.; Ghrefat, H.; Naeem, M. Hydrogeological vulnerability and pollution risk mapping of the Saq and overlying aquifers using the DRASTIC model and GIS techniques, NW Saudi Arabia. *Environ. Earth Sci.* **2015**, *74*, 1303–1318. [CrossRef]
28. Ijumulana, J.; Ligate, F.; Irunde, R.; Bhattacharya, P.; Ahmad, A.; Tomašek, I.; Maity, J.P.; Mtalo, F. Spatial variability of the sources and distribution of fluoride in groundwater of the Sanya alluvial plain aquifers in northern Tanzania. *Sci. Total. Environ.* **2022**, *810*, 152153. [CrossRef] [PubMed]
29. Abdelkader, M.; Al-amoud, A.; El, M.; El-feky, A. Remote Sensing Applications: Society and Environment Assessment of flash flood hazard based on morphometric aspects and rainfall-runoff modeling in Wadi Nisah, central Saudi Arabia. *Remote Sens. Appl. Soc. Environ.* **2021**, *23*, 100562.
30. Gomaa, H.; Alotibi, A.; Charni, M.; Almarri, A.; Gomaa, F. Conceptual Evaluation of Factors Controlling Groundwater Chemistry in Ad-Dawadmi, Saudi Arabia, Using Visualization and Multiple Lines of Evidence, Water (Switzerland). *Water* **2022**, *14*, 1857. [CrossRef]
31. Gomaa, H.; Charni, M.; Alotibi, A.A.; AlMarri, A.; Gomaa, F. Spatial Distribution, and Hydrogeochemical Factors Influencing the Occurrence of Total Coliform and E. coli Bacteria in Groundwater in a Hyperarid Area, Ad-Dawadmi, Saudi Arabia. *Water* **2022**, *14*, 3471. [CrossRef]
32. Ahmed, M.; Aqnouy, M.; El Messari, J.S. Sustainability of Morocco's groundwater resources in response to natural and anthropogenic forces. *J. Hydrol.* **2021**, *603*, 126866. [CrossRef]
33. El-Didy, S. Evaluation of The Proposed Drainage Network for Lowering the Groundwater Levels in Al-Dawadmi Town. *J. King Abdulaziz Univ. Environ. Arid L. Agric. Sci.* **1997**, *8*, 111–123. [CrossRef]
34. AdDawadmi_Gover. 2022. Available online: https://en.wikipedia.org/wiki/Dawadmi (accessed on 12 March 2022).
35. Timeanddate, Climate and Weather Averages in Ad Dawadmi, Saudi Arabia, Timeanddate. 2022. Available online: https://www.timeanddate.com/weather/saudi-arabia/dawadmi/climate (accessed on 12 March 2022).
36. Johnson, P.R. *Explanatory Notes To the Map of Proterozoic Geology of Western Saudi Arabia*; Saudi Geological Survey-Riyadh Office: Jeddah, Saudi Arabia, 2006.
37. Al Shanti, M.S. The Geology and Mineralization of the Ad-Dawadmi District of Saudi Arabia. Ph.D. Thesis, Imperial College London, London, UK, 1973.
38. El-Sawy, E.; Eldougdoug, A.; Gobashy, M. Geological and geophysical investigations to delineate the subsurface extension and the geological setting of Al Ji'lani layered intrusion and its mineralization potentiality, ad Dawadimi district, Kingdom of Saudi Arabia. *Arab. J. Geosci.* **2018**, *11*, 1–25. [CrossRef]
39. El-Sawy, E.; Masrouhi, A. Structural style and kinematic evolution of Al Ji'lani area, Ad Dawadimi terrane, Saudi Arabia. *J. African Earth Sci.* **2019**, *150*, 451–465. [CrossRef]
40. Quevauviller, P.; Thompson, K. *Analytical Methods for Drinking Water*; John Wiley & Sons, Ltd.: Hoboken, NJ, USA, 2005. [CrossRef]
41. UGSS. National Field Manual for the Collection of Water-Quality Data. In *U.S. Geological Survey Techniques of Water-Resources Investigations, Techniques of Water-Resources Investigations, Book 9*; U.S. Geological Survey: Reston, VA, USA, 2015. [CrossRef]
42. APHA. *Standard Methods: For the Examination of Water and Wastewater*, 23rd ed.; American Public Health Association: Washington DC, USA, 2017. [CrossRef]
43. Hussein, R.A. Study on Some Sources of Nitrate Pollution in Water Using Nitrogen-15 Isotope Technique. Master's Thesis, Ain Shams University, Cairo, Egypt, 2005.
44. Middleton, K.R. A new procedure for rapid determination of nitrate and a study of the preparation of the phenol-sulphonic acid reagent. *J. Appl. Chem.* **1958**, *8*, 505–509. [CrossRef]
45. Ahmed, M.; Aly, A.; Bastaweesy, A.; Gomaa, H. Modified Low-Priced Ammonia Diffusion Method for the Analysis of Nitrogen Isotopic Composition of Ammonium and Nitrate in Different Water Matrices. *Egypt J. Radiat. Sci. Appl.* **2006**, *21*, 257–281.
46. SBhat, A.; Cui, G.; Li, W.; Wei, Y.; Li, F. Effect of heavy metals on the performance and bacterial profiles of activated sludge in a semi-continuous reactor. *Chemosphere* **2020**, *241*, 125035. [CrossRef]
47. Karunanidhi, D.; Aravinthasamy, P.; Kumar, D.; Subramani, T.; Roy, P.D. Sobol sensitivity approach for the appraisal of geomedical health risks associated with oral intake and dermal pathways of groundwater fluoride in a semi-arid region of south India. *Ecotoxicol. Environ. Saf.* **2020**, *194*, 110438. [CrossRef] [PubMed]
48. Masoud, A.; Aldosari, A. Groundwater quality assessment of a multi-layered aquifer in a desert environment: A case study in wadi ad-dawasir, saudi arabia. *Water* **2020**, *12*, 3020. [CrossRef]
49. Zhang, Y.; Li, X.; Luo, M.; Wei, C.; Huang, X.; Xiao, Y.; Qin, L.; Pei, Q. Hydrochemistry and Entropy-Based Groundwater Quality Assessment in the Suining Area, Southwestern China. *J. Chem.* **2021**, *2021*, 5591892 . [CrossRef]
50. Sadat-Noori, M.; Ebrahimi, K. Groundwater vulnerability assessment in agricultural areas using a modified DRASTIC model. *Environ. Monit. Assess.* **2016**, *188*, 1–18. [CrossRef]

51. Bozdağ, A. Assessment of the hydrogeochemical characteristics of groundwater in two aquifer systems in Çumra Plain, Central Anatolia. *Environ. Earth Sci.* **2016**, *75*, 1–15. [CrossRef]
52. ArcMap, How IDW Works—Help | ArcGIS for Desktop. 2022. Available online: https://desktop.arcgis.com/en/arcmap/10.3/tools/3d-analyst-toolbox/how-idw-works.htm (accessed on 14 December 2022).
53. Mallick, J.; Singh, C.; AlMesfer, M.; Kumar, A.; Khan, R.; Islam, S.; Rahman, A. Hydro-geochemical assessment of groundwater quality in Aseer Region, Saudi Arabia. *Water* **2018**, *10*, 1847. [CrossRef]
54. Ahmad, A.; Al-Ghouti, M.; Khraisheh, M.; Zouari, N. Hydrogeochemical characterization and quality evaluation of groundwater suitability for domestic and agricultural uses in the state of Qatar. *Groundw. Sustain. Dev.* **2020**, *11*, 100467. [CrossRef]
55. Chadha, D.K. A proposed new diagram for geochemical classification of natural waters and interpretation of chemical data. *Hydrogeol. J.* **1999**, *7*, 431–439. [CrossRef]
56. Piper, A.M. A graphic procedure in the geochemical interpretation of water-analyses. *Transcation Am. Geophys. Union.* **1944**, *25*, 914–928. [CrossRef]
57. Lorenz, D. Piper Plot and Stiff Diagram Examples. 2016; pp. 1–9. Available online: https://pubs.usgs.gov/of/2016/1188/downloads/ofr20161188_appendix8.pdf (accessed on 15 January 2023).
58. Adimalla, N.; Li, P.; Venkatayogi, S. Hydrogeochemical Evaluation of Groundwater Quality for Drinking and Irrigation Purposes and Integrated Interpretation with Water Quality Index Studies. *Environ. Process.* **2018**, *5*, 363–383. [CrossRef]
59. AlSuhaimi, A.; AlMohaimidi, K.; Momani, K. Preliminary assessment for physicochemical quality parameters of groundwater in Oqdus Area, Saudi Arabia. *J. Saudi Soc. Agric. Sci.* **2019**, *18*, 22–31. [CrossRef]
60. Güler, C.; Thyne, G.; Mccray, J.; Turner, A. Evaluation of graphical and multivariate statistical methods for classification of water chemistry data. *Hydrogeol. J.* **2002**, *10*, 455–474. [CrossRef]
61. Chidambaram, S.; Anandhan, P.; Prasanna, M. Major ion chemistry and identification of hydrogeochemical processes controlling groundwater in and around Neyveli Lignite Mines, Tamil Nadu, South India. *Arab. J. Geosci.* **2012**, *6*, 3451–3467. [CrossRef]
62. Feth, R.; Gibbs, J.H. Mechanisms Controlling World Water Chemistry: Evaporation-Crystallization Process. *Am. Assoc. Adv. Sci. Stable.* **1971**, *172*, 870–872. [CrossRef]
63. Bouwer, H. Irrigation, and global water outlook. *Natl. Conf. Publ. Inst. Eng. Aust.* **1994**, *2*, 221–231. [CrossRef]
64. Schoeller, H. Qualitative Evaluation of Ground Water Resources. In *Methods and Techniques of Groundwater Investigation and Development*; Schoeller, H., Ed.; The United Nations Educational, Scientific and Cultural Organization: Paris, France, 1965; pp. 44–52.